



A globally distributed dataset of coseismic landslide mapping via multi-source high-resolution remote sensing images

Chengyong Fang¹, Xuanmei Fan¹, Xin Wang¹, Lorenzo Nava², Hao Zhong^{1,3}, Xiujun Dong¹, Jixiao Qi¹, and Filippo Catani²

¹State Key Laboratory of Geohazard Prevention and Geoenvironment Protection, Chengdu University of Technology, 610059 Chengdu, China

²Machine Intelligence and Slope Stability Laboratory, Department of Geosciences, University of Padua, 35129 Padua, Italy

³College of Information Science and Technology, Chengdu University of Technology, 610059 Chengdu, China

Correspondence: Xuanmei Fan (fxm_cdut@qq.com)

Received: 18 June 2024 – Discussion started: 18 July 2024

Revised: 4 September 2024 – Accepted: 9 September 2024 – Published: 24 October 2024

Abstract. Rapid and accurate mapping of landslides triggered by extreme events is essential for effective emergency response, hazard mitigation, and disaster management. However, the development of generalized machine learning models for landslide detection has been hindered by the absence of a high-resolution, globally distributed, event-based dataset. To address this gap, we introduce the Globally Distributed Coseismic Landslide Dataset (GDCLD), a comprehensive dataset that integrates multi-source remote sensing images, including PlanetScope, Gaofen-6, Map World, and uncrewed aerial vehicle (UAV) data, with varying geographical and geological background for nine events across the globe. The GDCLD data are freely available at <https://doi.org/10.5281/zenodo.13612636> (Fang et al., 2024). In this study, we evaluated the effectiveness of GDCLD by comparing the mapping performance of seven state-of-the-art semantic segmentation algorithms. These models were further tested by three different types of remote sensing images in four independent regions, with the GDCLD-SegFormer model achieving the best performance. Additionally, we extended the evaluation to a rainfall-induced landslide dataset, where the models demonstrated excellent performance as well, highlighting the dataset's applicability to landslide segmentation triggered by other factors. Our results confirm the superiority of GDCLD in remote sensing landslide detection modeling, offering a comprehensive database for rapid landslide assessment following future unexpected events worldwide.

1 Introduction

Landslides triggered by extreme events such as earthquakes and heavy precipitation are responsible for most of the damage to mountainous settlements (Huang and Fan, 2013). In some cases, landslides can be even more disastrous than the triggering events themselves as they can render emergency responses ineffective by cutting off roads and other transportation lifelines (Cigna et al., 2012; Huang et al., 2012; Valagussa et al., 2019; Chau et al., 2004). Therefore, the

rapid and accurate identification of landslides after extreme events is crucial for timely and quantitative assessment of disasters. This is especially important for emergency rescue operations and subsequent risk management in mountainous areas with complex environments and possibly inconvenient transportation routes (Cigna et al., 2018; Chau et al., 2004; Gorum et al., 2011).

Conventional landslide mapping efforts rely on traditional surveying methods such as topographic total stations, field observations to collect essential data on slope stability and

terrain morphology (Brardinoni et al., 2003; Coe et al., 2003; Zhong et al., 2020). These methods may not capture the full extent of terrain dynamics due to their static nature (Metternicht et al., 2005). Consequently, these methods are not effective for detailed landslide mapping, especially when traversing the affected and unstable regions for field surveys is not possible. This was particularly true for the Wenchuan co-seismic landslides, which mobilized large amounts of material that obstructed roads, complicating disaster response efforts as well as surveying and mapping activities (Gorum et al., 2011). With the development of remote sensing technology in the past decades, landslide investigation has been supported by digital mapping, which reduces time and labor costs (Fiorucci et al., 2011, 2019; Gao and Maro, 2010; Guzzetti et al., 2012). This mapping has also been enhanced by various modalities of sensors, such as synthetic aperture radar (Mondini et al., 2021; Nava et al., 2021), multi-spectral (Udin et al., 2019), and hyper-spectral (Ye et al., 2019) imagery. However, visual identification is highly subjective due to operator experience, and the interpretation of events involving numerous landslides is still time-consuming. Therefore, this subjectivity and the time-consuming nature of interpretation hinder the reliability and efficiency of landslide mapping, for example, after major events such as the Wenchuan, China (2008), and Gorkha, Nepal (2015), earthquakes.

Generally, the ideal solution is to develop automated models or tools that can save time and costs while ensuring an objective protocol in the mapping process (Casagli et al., 2023). While some researchers have endeavored to employ machine learning or deep learning in constructing these models, most of them lack the generalization capability for application across diverse environmental backgrounds and remote sensing images (Burrows et al., 2019; Bhuyan et al., 2023; Li et al., 2016; Liu et al., 2022; Lu et al., 2019; Luppino et al., 2022; Meena et al., 2021; Soares et al., 2022; Yang et al., 2022b; Mohan et al., 2021; Ss and Shaji, 2022; Li et al., 2024). To improve such models, more abundant data that consider the diverse geomorphological and climatic settings where landslides occur are essential. The Bijie landslide dataset, based on Map World imagery, presents a small-scale dataset of mountainous landslides, filling the gap in landslide detection tasks for the first time (Ji et al., 2020). Landslide4Sense, based on Sentinel-2 imagery, introduces a multi-spectral landslide dataset, pioneering semantic-level annotation of landslides (Ghorbanzadeh et al., 2022). The HR-GLDD and GVLM datasets, based on PlanetScope and Google Earth imagery, respectively, represent global-scale high-resolution landslide datasets (Meena et al., 2023; Zhang et al., 2023). However, these datasets are limited by their reliance on a single remote sensing data source, restricting the applicability of models across different sensors and resolutions. The CAS Landslide dataset introduces a mountain landslide dataset containing various remote sensing data sources (Xu et al., 2024). However, due to its limited an-

notated landslide quantity, high image overlap, and lack of negative samples (background/non-landslide), it is still insufficient to effectively generalize to automatic landslide mapping tasks in various complex environments, especially where signatures of landslides often resemble nearby terrain.

Therefore, there is an urgent need to develop a carefully curated and diverse dataset. Such a dataset would facilitate the rapid and accurate mapping of landslides using available prior knowledge. Hence, we present a comprehensive landslide dataset derived from nine earthquake-triggered landslide events, encompassing multi-sensor images from 3 m PlanetScope, 2 m Gaofen-6, 0.5 m Map World, and 0.2 m uncrewed aerial vehicle (UAV). This work addresses the shortcomings of existing datasets in terms of accuracy and generalization for training large and complex deep learning models. It is of great significance for accurate, rapid, and automatic mapping of landslides occurring anywhere in the world, providing strong support for efficient geohazard emergency response and investigation.

The paper is structured as follows: Sect. 2 reviews existing high-quality landslide datasets to provide an overview of the current state of research. Section 3 introduces the data collection and preparation process to showcase the extensive research events and scientific methodology behind our data production. Section 4 describes the semantic segmentation algorithms, loss functions, and parameter settings used in this study and shows the rationale behind their use. Section 5 presents the results, including the training, validation, and testing outcomes of the dataset, as well as the generalization ability of the model trained by the Globally Distributed Coseismic Landslide Dataset (GDCLD) in independent regions. Section 6 discusses the innovation and effectiveness of GDCLD, illustrating its effective application in several landslide events.

2 Related work

The most effective approach to landslide mapping currently involves image segmentation, and computer vision segmentation tasks depend heavily on high-quality data to build accurate models. However, landslide segmentation tasks have developed relatively recently compared to other computer vision applications, resulting in only a limited number of studies that have constructed datasets for various landslide events. In this section, we review some of these landslide segmentation datasets and provide detailed information on each (Table 1).

The Bijie landslide dataset comprises high-resolution satellite images captured in landslide-prone areas of Guizhou province, China. The dataset includes 770 landslide samples and 2003 non-landslide samples. The positive samples consist of rockfalls, rockslides, and a small number of debris avalanches, while the negative samples include mountains, villages, roads, rivers, and farmland among others. The im-

age resolutions vary from 61×61 to 1239×1197 pixels, with RGB channels. There are a total of 7.23×10^6 pixels assigned to landslide within the dataset (Ji et al., 2020).

The Landslide4Sense dataset consists of multi-spectral satellite images captured across four distinct regions. This dataset comprises 3799 images, each with a dimension of 64×64 pixels and a spatial resolution of 10 m. Each image contains 14 bands, including 12 bands from the Sentinel-2 satellite and two bands from digital elevation model (DEM) data. The dataset includes negative background samples such as bare soil, rivers, and buildings. There are a total of 1.76×10^6 pixels assigned to landslides within the dataset (Ghorbanzadeh et al., 2022).

The HR-GLDD spans 10 distinct geographic regions, capturing landslide instances across various geographical environments in south Asia, southeast Asia, east Asia, South America, and Central America. HR-GLDD comprises a total of 1756 image patches, each standardized to a size of 128×128 pixels, with a spatial resolution of up to 3 m. The dataset is sourced from four spectral bands of the PlanetScope satellite. It includes a variety of negative samples, such as non-landslide terrain features, buildings, and roads, ensuring a comprehensive representation for model training. There are a total of 2.96×10^6 pixels assigned to landslides within the dataset (Meena et al., 2023).

The GVLM dataset spans six continents and 17 different landslide sites. GVLM covers a diverse range of geological and climatic conditions, from the lush landscapes of Asia to the rugged terrain of South America. Comprising 17 pairs of dual-temporal very high-resolution (VHR) images, each image pair boasts a spatial resolution of 0.59 m, ensuring a detailed capture of landslide features and their surrounding environments. GVLM incorporates various negative samples, including non-landslide landforms, infrastructure such as buildings, and transportation networks, providing a holistic training ground for models. Image sizes within the GVLM dataset range from 1861×1749 to 10828×7424 pixels. There are a total of 3.24×10^7 pixels assigned to landslides within the dataset (Zhang et al., 2023).

The CAS Landslide dataset covers nine different geographic regions spanning south Asia, southeast Asia, east Asia, South America, and Central America. Comprising 20 865 image patches, each standardized to a size of 512×512 pixels, the dataset offers a spatial resolution ranging from 0.2 to 5 m. During the cropping process, an overlap setting parameter of 0.5 was used. These images are sourced from uncrewed aerial vehicles (UAVs) and satellite platforms, integrating data from the PlanetScope satellite and other sources. The dataset removes background images that do not contain landslide pixels and therefore lacks sufficient background noise as negative samples to enhance the robustness of the model. There are a total of 1.95×10^8 pixels assigned to landslides within the dataset (Xu et al., 2024).

In summary, comparing with other remote sensing detection tasks such as land cover/use, the currently available land-

slide datasets are exceedingly scarce, predominantly comprising single remote sensing images with low spatial resolutions. Most crucially, these datasets lack sufficient annotations of landslide instances, exhibit high overlap, and suffer from a dearth of diverse negative samples. As a result, they are ill-equipped to tackle the challenges of mapping landslides in large-scale areas with complex background objects, especially those sharing spectral and textural characteristics with landslide surfaces, such as bare soil and rocks. Furthermore, they fail to provide adequate data sources for effectively training large-scale neural network baseline models.

3 Globally Distributed Coseismic Landslide Dataset (GDCLD)

The creation of the GDCLD dataset can be broadly divided into two main components: landslide data collection and remote sensing data processing. In the first part, we compiled recent landslide events triggered by earthquakes worldwide over the past 7 years and obtained the corresponding remote sensing images. The second part details the process of annotating landslide labels and the methodology used to create the standard dataset. The workflow is illustrated in Fig. 1.

3.1 Data collection

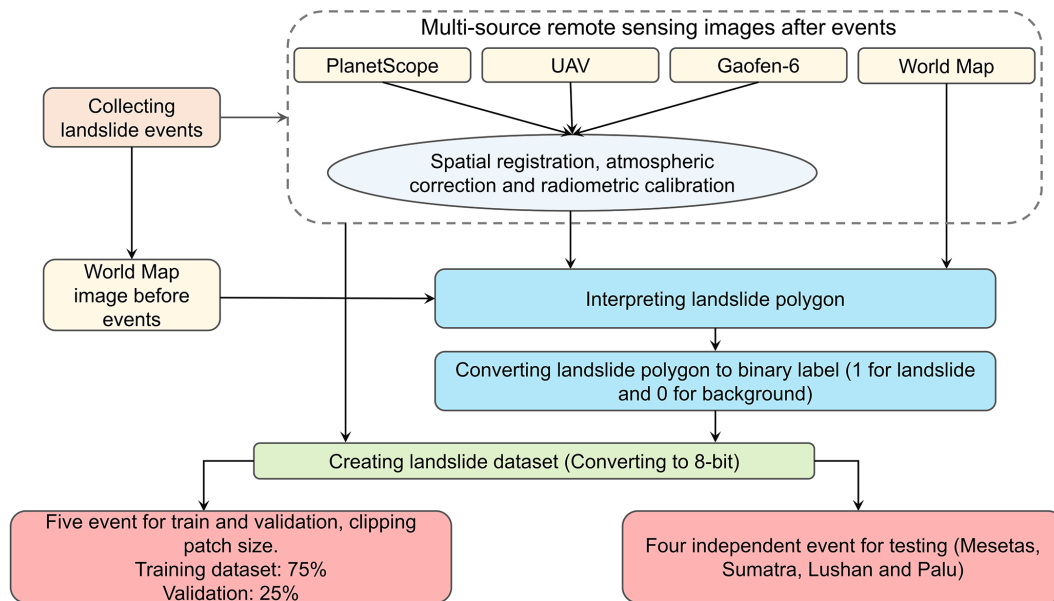
Our dataset encompasses a catalog of landslides triggered by nine seismic occurrences delineated across the Himalayan seismic belt and the Circum-Pacific belt as depicted in Fig. 2. These regions have actively witnessed seismic events with magnitudes over 5.9, triggering numerous landslides (Table 2). We obtained data of these locations from various remote sensing sources. This section delineates the particulars of the seismic events and the provenance of the remote sensing data.

3.1.1 The 2017 Jiuzhaigou earthquake-triggered landslides

On 8 August 2017, a M_w 6.5 earthquake struck Jiuzhaigou in Sichuan province, China (102.82° E, 33.20° N), triggering 2498 landslides that were predominantly shallow surface slides and collapses. The largest landslide covered approximately 2.3×10^5 m² (Fan et al., 2018). Jiuzhaigou, situated on the northeastern margin of the Qinghai–Tibet Plateau within the tectonically active zone north of the Longmenshan fault, is part of the Mediterranean–Himalayan seismic belt (Fan et al., 2018). The region's average elevation exceeds 3000 m with a maximum relief of 2228 m and a vegetation cover surpassing 70 % (Yi et al., 2020; Chen et al., 2019). Exposed geological formations include various gray–white sandstones and dolomites from the Devonian, Carboniferous, Permian, Triassic, and Tertiary periods (Fang et al., 2022). After the earthquake, we acquired multiple remote sensing images: a 0.2 m resolution UAV image (Phase One iXU1000)

Table 1. Existing landslide dataset statistics.

Dataset	Bands	Events	Tiles	Landslide number	Labeling pixels
Bijie landslide	3	1	2773	770	7.23×10^6
Landslide4Sense	14	4	3799	> 30 000	1.76×10^6
HR-GLDD	4	13	1756	7193	2.96×10^6
GVLN	3	17	17	–	3.24×10^7
CAS Landslide	3	9	20 865	–	1.95×10^8

**Figure 1.** The workflow of producing GDCLD.

on 22 September 2017, a 3 m resolution PlanetScope image on 13 October 2017, and a 0.5 m resolution from Map World (Fig. S1 in the Supplement).

PlanetScope images on 17 December 2017 and 8 April 2018 to interpret the landslides (Fig. S2).

3.1.2 The 2017 Mainling earthquake-triggered landslides

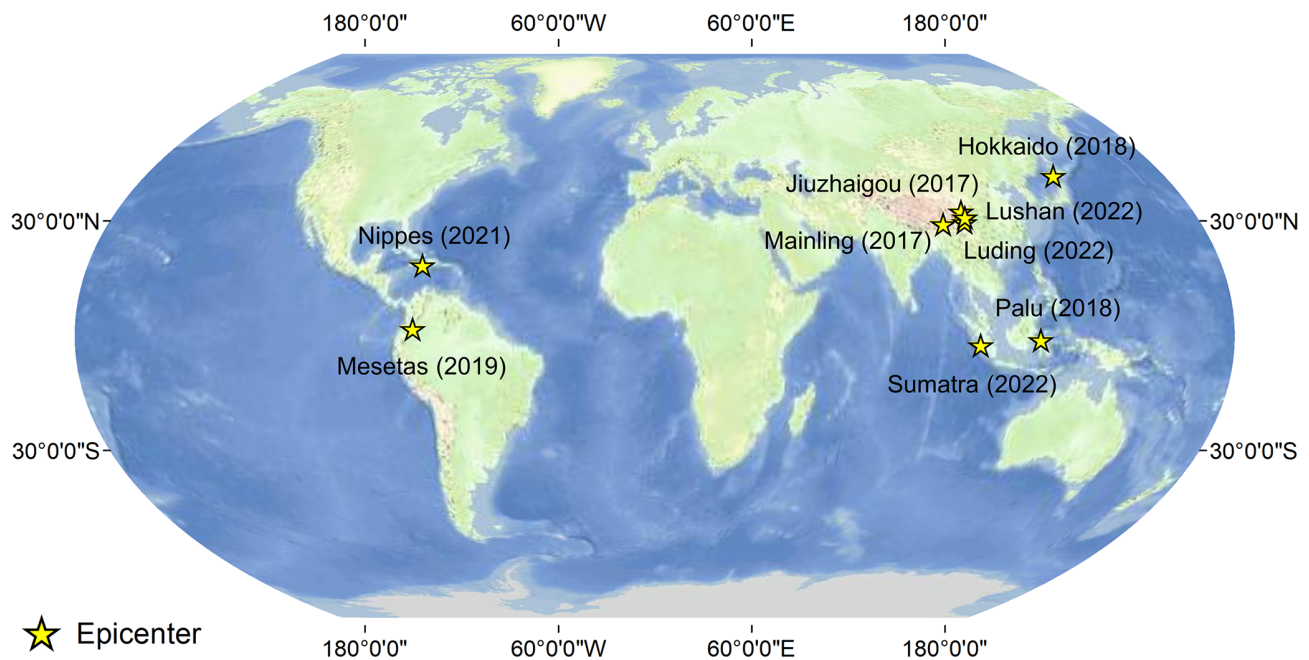
On 18 November 2017, a magnitude 6.4 earthquake struck Mainling (95.02° E, 29.75° N), resulting in three injuries and affecting 12 000 individuals. The earthquake triggered over 1000 landslides, obstructing numerous watercourses and covering a total area of 33.61 km², with the largest landslide spanning 4.9 km² (Hu et al., 2019). Mainling, located on the southeastern margin of the Qinghai–Tibet Plateau within the Yarlung Zangbo Grand Canyon, is part of the Mediterranean Himalayan seismic zone. This region, with altitudes ranging from 800 to 7782 m and an average elevation of 2500 m, features a maximum elevation differential of 2000 m and a robust vegetation coverage of 60 % (Gao et al., 2023; Chen et al., 2019). The monsoonal climate here brings annual rainfall of between 1500 and 2000 mm (Huang et al., 2021). Following the earthquake, we acquired 3 m resolution

3.1.3 The 2018 Hokkaido earthquake

On 6 September 2018, a M_w 6.6 earthquake struck Hokkaido, Japan (142.01° E, 42.69° N), resulting in 44 fatalities and over 660 injuries. Approximately 80 % of the casualties were due to coseismic landslides. The earthquake triggered over 7800 landslides, causing extensive damage to infrastructure. The total area affected by landslides was 23.77 km², with the largest individual landslide covering 0.5 km² (Wang et al., 2019). The region, which receives an annual precipitation of 1200–1800 mm – relatively low compared to other parts of Japan (Yamagishi and Yamazaki, 2018) – is characterized by sandstone, mudstone, siltstone, and shale formations overlaid by substantial volcanic sediments (Wang et al., 2019). Following the Hokkaido earthquake, we acquired PlanetScope imagery with a 3 m resolution on 12 December 2018 and Map World imagery with a 0.5 m resolution (Fig. S3).

Table 2. Summary table of landslide event information in GDCLD.

Events	M_w	Time	Geographic coordinates	Landslide number	Total landslide area [km ²]
Jiuzhaigou	6.5	2017	(102.82° E, 33.20° N)	2498	14.5
Mainling	6.4	2017	(95.02° E, 29.75° N)	1448	33.6
Hokkaido	6.6	2018	(142.01° E, 42.69° N)	7962	23.8
Palu	7.5	2018	(119.84° E, 0.18° S)	15 700	43.0
Mesetas	6.0	2019	(76.19° W, 3.45° N)	804	8.5
Nippes	7.2	2021	(73.45° W, 18.35° N)	4893	45.6
Sumatra	6.1	2022	(100.10° E, 0.22° N)	602	10.6
Lushan	5.9	2022	(102.94° E, 30.37° N)	1063	7.2
Luding	6.8	2022	(102.08° E, 29.59° N)	15 163	28.53

**Figure 2.** Distribution of earthquake-triggered landslide events.

3.1.4 The 2018 Palu earthquake

On 28 September 2018, the Palu region of Sulawesi, Indonesia, was struck by a M_w 7.5 earthquake with a focal depth of 10 km (0.18° S, 119.84° E). A detailed analysis by Shao et al. (2023) identified approximately 15 700 coseismic landslides across a 14 600 km² area, with a combined landslide area of about 43.0 km². These landslides were predominantly concentrated in the mountainous canyon regions south of the epicenter. This study provides a semantic-level interpretation of these landslides, which were mainly shallow disruptions (Shao et al., 2023). However, some larger-scale flow slides, rockfalls, and debris flows were also observed. High-resolution Map World imagery (1 m) was utilized to support this analysis (Fig. S4).

3.1.5 The 2019 Mesetas earthquake

The research site is located in the eastern foothills of the Colombian Eastern Cordillera. On 24 December 2019, the Mesetas earthquake, with a magnitude of 6.0, struck this region as documented by Poveda et al. (2022). The earthquake's epicenter was located at 76.19° W, 3.45° N, triggering approximately 800 coseismic landslides. The distribution and predominant orientation of these landslides were influenced by the shear zone confined within the Guapequito Fault, a subsidiary offshoot of the Algeciras Fault (Poveda et al., 2022). High-resolution PlanetScope images (3 m) were acquired on 5 January and 12 February 2020 to analyze these phenomena (Fig. S5).

3.1.6 The 2021 Nippes earthquake

On 14 August 2021, a M_w 7.2 earthquake struck the Nippes mountains in Haiti (73.45° W, 18.35° N). This seismic event, compounded by heavy rainfall from Hurricane Grace on 16–17 August, triggered numerous secondary geological hazards across the Tiburon Peninsula. The disaster resulted in at least 2246 fatalities and injured over 12 763 individuals (Calais et al., 2022). There were a total of 4893 earthquake-induced landslides, covering an estimated 45.6 km², with the largest individual landslide spanning 3.1×10^5 m² (Zhao et al., 2022b). The affected area, with elevations of up to 2300 m (Alpert, 1942), consists mainly of volcanic rocks, such as basalts, and sedimentary formations, particularly limestones (Harp et al., 2016). After the earthquake, we utilized 3 m resolution PlanetScope imagery (29 August 2022) and 0.5 m resolution Map World imagery to assess the damage (Fig. S6).

On 14 August 2021, a seismic event registering M_w 7.2 hit in the Nippes mountains of Haiti (73.45° W, 18.35° N). This seismic activity coupled with substantial rainfall from Hurricane Grace between 16 and 17 August precipitated a significant number of secondary geological hazards in the Tiburon Peninsula. The calamity resulted in a tragic loss of at least 2246 lives and inflicted injuries upon more than 12 763 individuals (Calais et al., 2022). The earthquake triggered a total of 4893 landslides, covering an estimated area of 45.6 km², with the maximum individual area reaching 3.1×10^5 m² (Zhao et al., 2022b). The study area, characterized by elevations reaching up to 2300 m above sea level (Alpert, 1942). Comprised predominantly of volcanic rocks, such as basalts, and sedimentary formations, notably limestones (Harp et al., 2016). In addition to obtaining 3 m resolution PlanetScope imagery after the Nippes earthquake, we also acquired 0.5 m resolution Map World imagery (Fig. S6).

3.1.7 The 2022 Sumatra earthquake

On 25 February 2022, a M_w 6.1 earthquake struck West Sumatra, Indonesia, at a shallow depth of 4.9 km. The epicenter was located approximately 20 km from Mount Talakmau (100.10° E, 0.22° N), a compound volcano rising to about 3000 m. Mount Talakmau, active during the Holocene, consists of andesite and basalt from the Pleistocene–Holocene epochs (Basofi et al., 2016). The earthquake induced extensive landslides over a 6 km² area on the volcano's eastern and northeastern flanks. High-resolution PlanetScope imagery (3 m) from 5 March and 24 April 2022 captured these landslides (Fig. S7).

3.1.8 The 2022 Lushan earthquake

On 1 June 2022, a M_w 5.9 earthquake (102.94° E, 30.37° N) struck Lushan County, China, resulting in four fatalities and 42 injuries, affecting 14 427 individuals. The seismic event triggered 1063 landslides over a total area of 7.2 km²,

with the largest landslide covering 0.3 km² (Zhao et al., 2022a). This region, located on the southeast margin of the Qinghai–Tibet Plateau, features an average elevation exceeding 2000 m, with altitudes ranging from 557 to 4115 m (Tang et al., 2023). It is characterized by lush vegetation covering 80 % of the area and experiences a subtropical monsoon climate with annual rainfall of between 1100 and 1300 mm (Chen et al., 2019). The geological composition predominantly consists of exposed sandstones and mudstones (Zhao et al., 2022a). High-resolution imagery, including 3 m resolution PlanetScope images, 0.5 m resolution Map World images, and 0.2 m resolution UAV images acquired on 13 June 2022 was collected using a Sony ILCE-5100 for the affected region (Fig. S8).

3.1.9 The 2022 Luding earthquake

On 5 September 2022, a M_w 6.8 earthquake struck Luding County, China (102.08° E, 29.59° N), resulting in 93 fatalities. The seismic event triggered approximately 15 000 landslides over an area of 28.53 km², with the largest individual landslide covering 2.4×10^5 m² (Dai et al., 2023). This region lies on the southeastern margin of the Qinghai–Tibet Plateau within the Y-shaped Xianshuihe fault system (Yang et al., 2022a). The geological composition predominantly includes limestone, sandstone, dolomite, and some intrusive rocks (Dai et al., 2023). In the aftermath of the earthquake, rapid rescue operations and data collection were undertaken, utilizing 0.2 m resolution UAV imagery (acquired on 7 October 2022 via Phase One IXU1000), PlanetScope imagery (3 m) (acquired on 25 September 2022), Map World imagery (0.5 m), and Gaofen-6 imagery (2 m) (Fig. S9).

3.2 Preprocessing of landslide dataset

In the aforementioned nine events, the available public data primarily focused on geological analysis rather than tasks related to semantic segmentation. After performing multi-source data spatial registration, atmospheric correction, and radiometric calibration on remote sensing images, we used QGIS for landslide interpretation. These labels were delineated with reference to pre-earthquake remote sensing imagery and post-earthquake multi-source remote sensing image. By comparing spectral disparities and analyzing morphological attributes between bi-temporal images, we mapped the semantic landslide labels. (Fig. 3). The mapping of landslide polygons for these nine events was primarily conducted by a team of five researchers, including the authors. All team members possess expertise in geology or remote sensing and were involved in a year-long process of detailed interpretation.

Moreover, we actively participated in the emergency response and field investigation after these major earthquakes in China. This further improved the reliability of the landslide inventories. Figure 4 showcases photographs captured

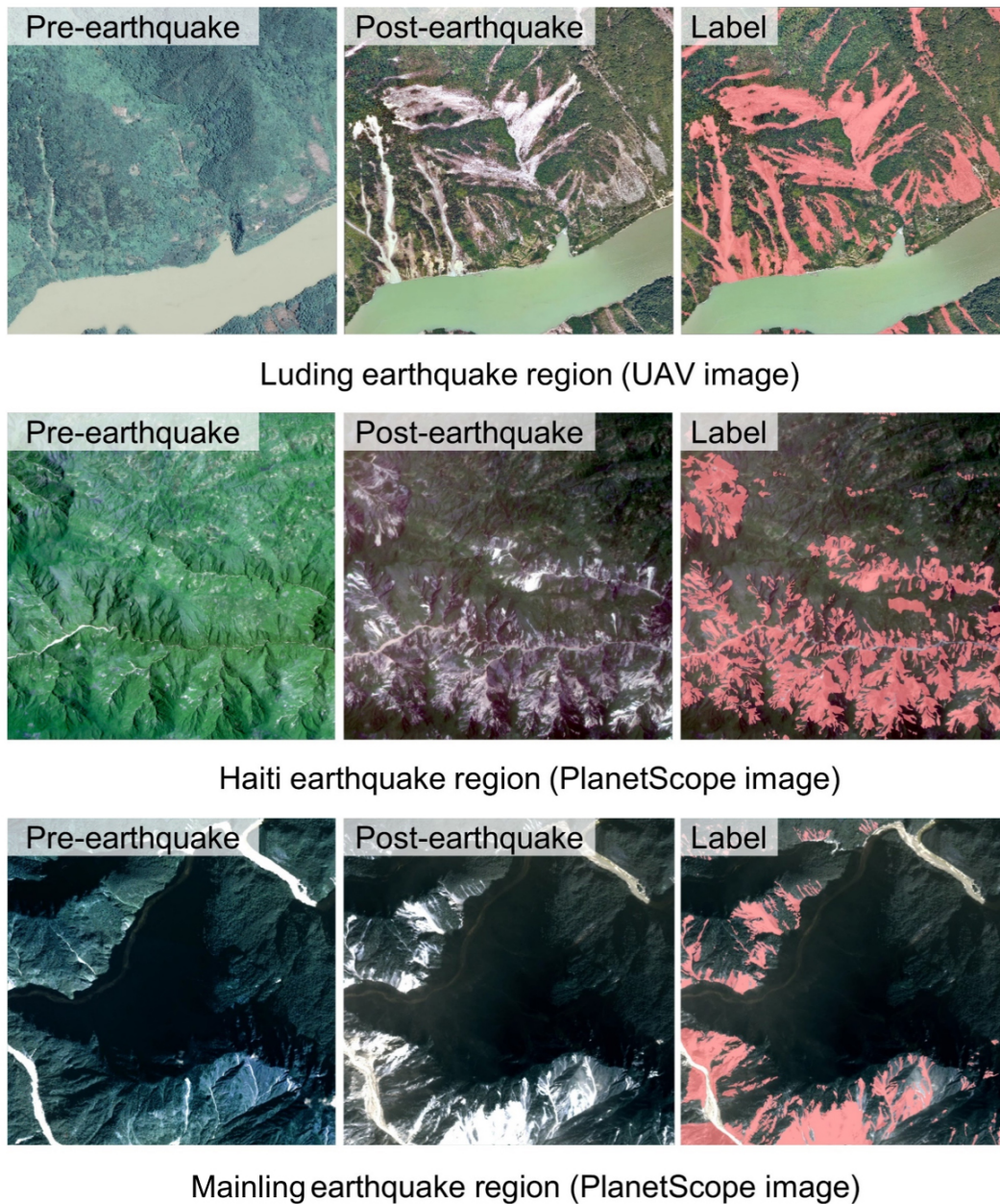


Figure 3. Remote sensing images before and after the earthquake and landslide interpretation results (landslides marked in red).

on site after the Jiuzhaigou earthquake, Lushan earthquake, and Luding earthquake. Specifically, Fig. 4a1 and b1 were taken in Luding, Sichuan, depicting the extensive devastation caused by concentrated coseismic landslides, impacting the village of Wandonghe and resulting in severe destruction of local infrastructure. Corresponding aerial photos with a resolution of 0.2 m (Fig. 4a2 and b2) offer a comprehensive perspective of the affected area. Figure 4c1, taken in Lushan, Sichuan, captures the consequences of the earthquake-triggered large landslide dam, which obstructed the river channel. The corresponding PlanetScope image,

Fig. 4c2, provides an overhead view of the altered landscape. Furthermore, Fig. 4d1, taken at the Jiuzhaigou Panda Sea, illustrates a significant volume of landslide deposits reaching the sea, with the accompanying UAV image at a resolution of 0.2 m (Fig. 4d2), offering detailed insights. Lastly, Fig. 4e presents a fieldwork photo involved in these surveys. These field investigations serve to enhance comprehension and subsequent calibration on our remote sensing interpretation.

To obtain semantic-level annotations for landslide labels, all remote sensing images were converted into RGB images (8 bit). The preprocessing stage was conducted through

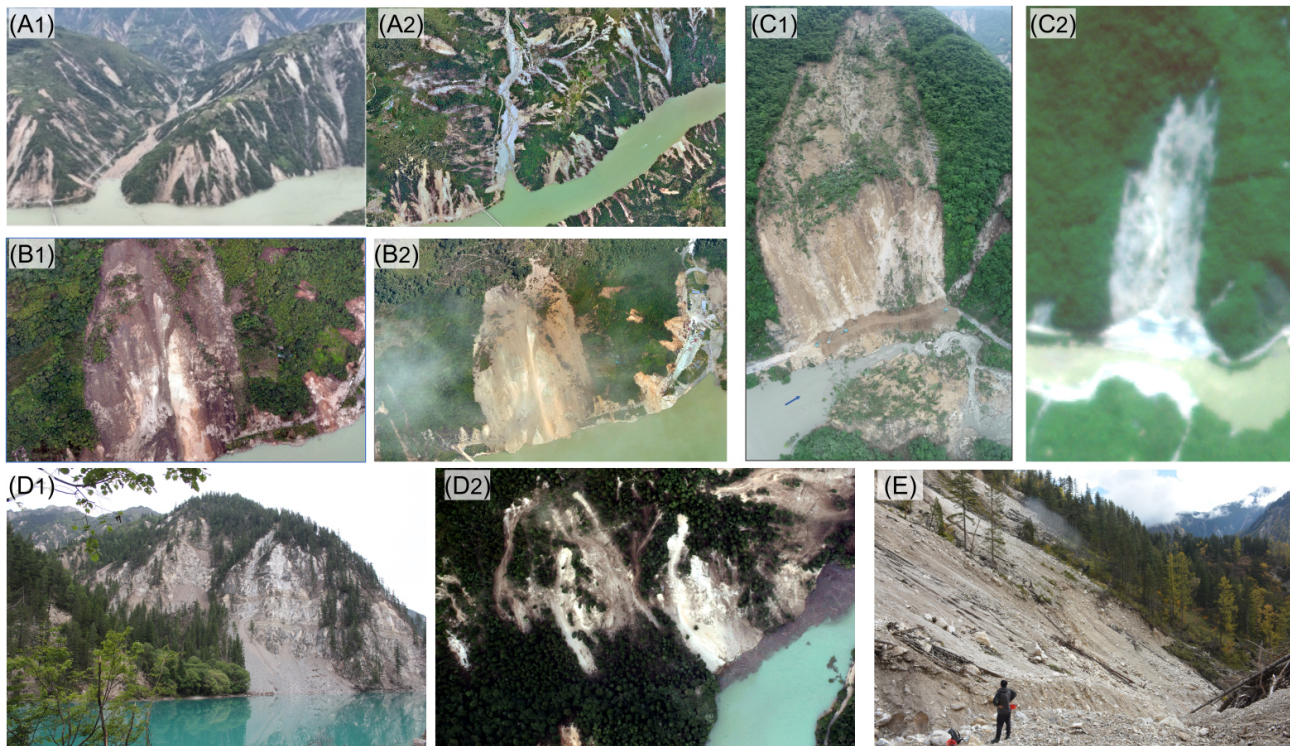


Figure 4. Comparison of field survey photos and remote sensing images: panels (a1) and (a2) show the Wandong landslides induced by the 2022 Luding earthquake, (b1) and (b2) show the Dadu River bridge landslide induced by the 2022 Luding earthquake, (c1) and (c2) show the Baoxing landslides induced by the 2022 Lushan earthquake, (d1) and (d2) show the Panda sea landslides induced by the 2017 Jiuzhaigou earthquake, and (e) shows a photo of fieldwork at Jiuzhaigou.

three steps: binary mask generation, data sampling, and image patching. First, utilizing the Rasterio library in Python, landslide vector labels for each selected region were transformed into binary masks, where 1 denoted a landslide and 0 represented the background. Subsequently, regions densely populated with landslides were sampled, and both remote sensing images and masks were patched and cropped into regular grids, yielding patches of 1024×1024 pixels. To mitigate interference among patches, the overlap parameter was set to 0. Given the obvious imbalance between non-landslide and landslide areas, we manually removed most of the images without any landslide pixel annotations. The ratios of positive landslide samples and negative non-landslide samples were 8.01 % and 91.99 %, respectively. Table 3 presents detailed information regarding different remote sensing data sources for each study case.

Additionally, to enhance the robustness and generalization capability of deep learning models, a subset of background noise elements such as clouds, roads, buildings, bare land, and rocks were manually selected as negative non-landslide samples. The negative samples can be outlined as follows: diverse roads (Fig. 5e, k, m, n, p, and s), river channels (Fig. 5e, k, n, s, and t), clouds (Fig. 5o and r), and barren land (Fig. 5c, h, and q). Additionally, human-engineered structures and buildings are also considered (Fig. 5e and k).

4 Experimental setup

After the completion of dataset construction, the experimental phase follows. In this section, we introduce several semantic segmentation algorithms used for validating the dataset, the loss functions and accuracy evaluation metrics employed in the experiments, as well as various hyperparameter settings utilized during the experiments.

4.1 Segmentation algorithms

In this section, we have selected seven of the most popular semantic segmentation networks, including four models based on the CNN architecture and three based on the transformer architecture. These seven algorithms have medium- to large-scale parameter sizes and computational complexities, and show excellent performance in a variety of remote sensing semantic scenarios, making them suitable for precision comparison and validation of novel datasets.

1. *U-Net*. As one of the earliest and most renowned semantic segmentation models, U-Net is distinguished by its unique U-shaped architecture (Ronneberger et al., 2015). This design facilitates efficient learning and precise localization by combining high-resolution features from the contracting path with upsampled outputs from

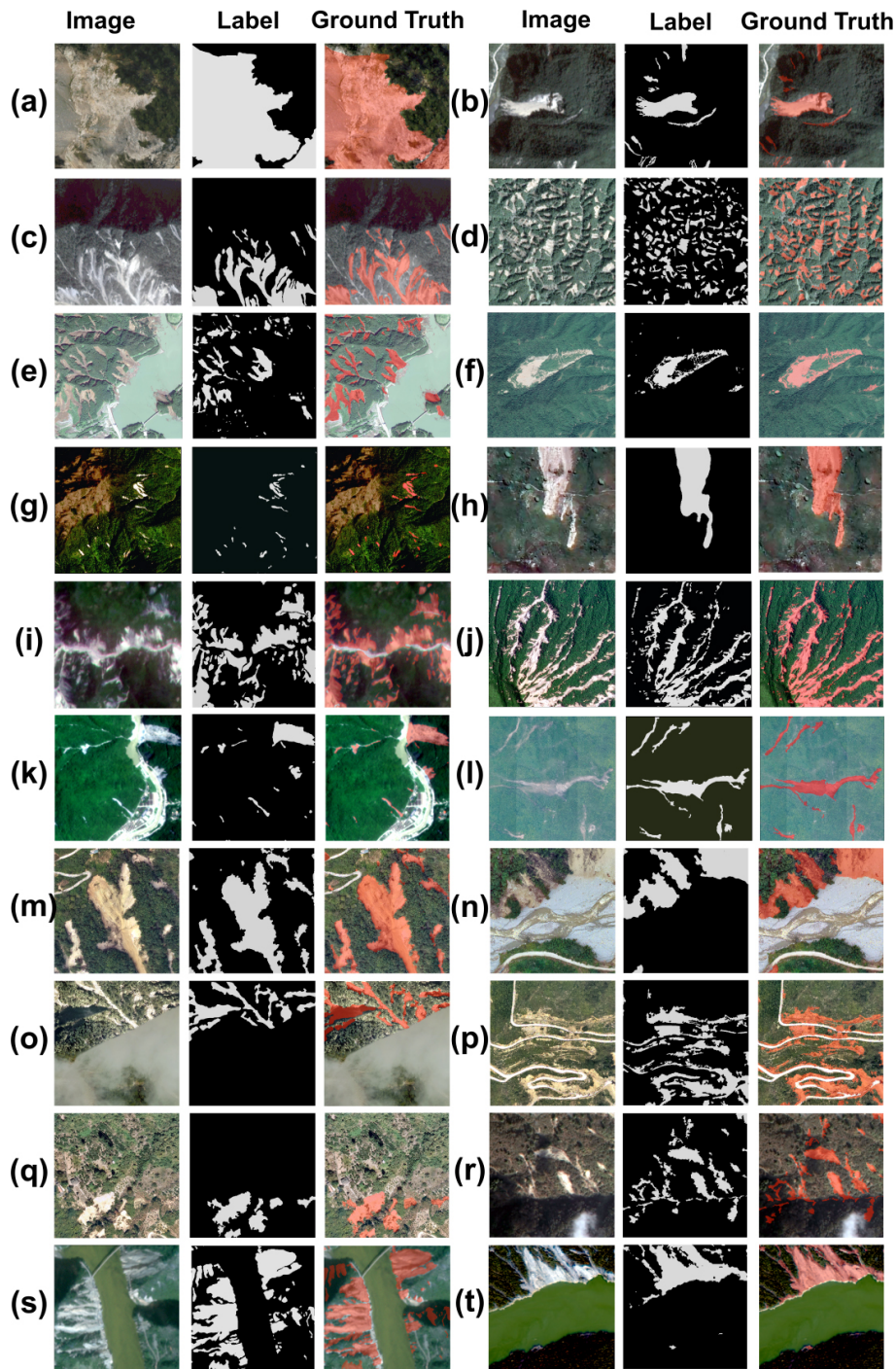


Figure 5. Display of landslide sample data from different study areas and different remote sensing data sources: Jiuzhaigou UAV (a), Jiuzhaigou PlanetScope (b), Mainling PlanetScope (c), Hokkaido PlanetScope (d), Hokkaido Map World (e), Palu Map World (f), Mesetas PlanetScope (g), Haiti Map World (h), Haiti PlanetScope (i), Sumatra PlanetScope (j), Lushan PlanetScope (k), Lushan UAV (l), Luding UAV (m–q), Luding Map World (r), Luding PlanetScope (s), and Luding Gaofen-6 (t). The “Label” column refers to the binary landslide mask, whereas the “Ground Truth” column illustrates the concordance between the annotated and actual landslide in images.

Table 3. Detailed information of each event in GDCLD.

Events	Data sources	Resolution	Number of tiles
Jiuzhaigou, 2017 (M_w of 6.5)	UAV	0.2 m	2288
	PlanetScope	3 m	176
Mainling, 2017 (M_w of 6.4)	PlanetScope	3 m	118
Hokkaido, 2018 (M_w of 6.6)	Map World	0.5 m	796
	PlanetScope	3 m	123
Palu, 2018 (M_w of 7.5)	Map World	1 m	335
Mesetas, 2019 (M_w of 6.0)	PlanetScope	3 m	144
Haiti, 2021 (M_w of 7.2)	PlanetScope	3 m	238
	Map World	0.5 m	404
Sumatra, 2022 (M_w of 6.1)	PlanetScope	3 m	110
Lushan, 2022 (M_w of 5.9)	UAV	0.2 m	210
	Map World	0.5 m	182
	PlanetScope	3 m	110
Luding, 2022 (M_w of 6.6)	UAV	0.2 m	9252
	Map World	0.5 m	1540
	Gaofen-6	2 m	496
	PlanetScope	3 m	190
Sum	–	–	16 712

the expanding path. Both the encoder and the decoder in U-Net are composed purely of convolutional neural networks (CNNs) structures (O’Shea and Nash, 2015). This simplicity, along with a relatively small number of parameters, allows U-Net to achieve exceptional accuracy and rapid inference using small datasets. Consequently, it is widely utilized in applications such as small-scale object classification, change detection, and medical imaging.

2. *ResU-Net*. ResU-Net is an advanced variant of the U-Net model, incorporating residual connections to enhance its performance and learning efficiency (Diakogiannis et al., 2020). The key innovation in ResU-Net is the integration of residual blocks within both encoder and decoder paths, which addresses the vanishing gradient problem and enables the training of deeper networks (He et al., 2016). These residual blocks allow the network to learn identity mappings, facilitating gradient flow through the network and improving convergence rates. Similar to U-Net, ResU-Net maintains a U-shaped architecture that combines high-resolution features from the contracting path with upsampled outputs from the expanding path, ensuring precise localization and context capture. The combination of residual connections improves feature reuse and learning efficiency, enabling ResU-Net to effectively improve recall and

small-target detection capabilities in semantic segmentation tasks.

3. *DeepLabV3*. DeepLabV3 is a semantic segmentation model known for its sophisticated use of atrous convolution or dilated convolution (Chen et al., 2018). This technique allows the network to capture multi-scale contextual information without losing the spatial resolution, addressing the limitations of traditional convolutional networks in dense prediction tasks. DeepLabV3 incorporates atrous spatial pyramid pooling to robustly segment objects at multiple scales by applying atrous convolution with different rates in parallel. This model also integrates features from both encoder and decoder paths, enhancing the precision of boundary delineation. In addition, the architecture of DeepLabV3 utilizes batch normalization and depth-separable convolution. This design can effectively reduce the complexity and computational cost of the model while enabling the model to have stronger feature extraction capabilities and generalization than simple networks such as U-Net.
4. *HRNet*. High-Resolution Net (HRNet) is noted for its innovative approach to maintaining high-resolution representations throughout the network (Wang et al., 2020). Unlike traditional models that gradually down-sample the input to extract features, HRNet preserves high-resolution features by maintaining parallel high- and low-resolution subnetworks. This design allows HRNet

to integrate multi-scale information effectively, ensuring precise localization and robust feature representation. The network continuously exchanges information across different resolutions, resulting in superior accuracy and detailed segmentation results. Due to its ability to retain fine-grained spatial information and adapt to various scales, HRNet excels in complex tasks such as fine-grained terrain classification, semantic segmentation in urban scenes, and fine-grained visual detection.

5. *UPerNet*. UPerNet employs a pyramid feature extraction method, integrating multi-scale information to capture contextual details across different resolutions (Xiao et al., 2018; Liu et al., 2022). It utilizes a feature pyramid network (FPN) backbone for hierarchical feature extraction, enhanced by a global context integration module to enrich overall scene understanding. Additionally, UPerNet incorporates lateral connections for efficient communication between feature pyramid levels, ensuring seamless information flow and accurate segmentation. This sophisticated architecture enables UPerNet to achieve superior segmentation performance, particularly in challenging scenarios with complex scenes and diverse object scales.
6. *SwinU-Net*. Built upon the Swin transformer architecture, SwinU-Net blends self-attention mechanisms with U-Net for exceptional performance (Cao et al., 2022). It inherits Swin transformer's hierarchical feature extraction for capturing both local and global contextual information efficiently (Liu et al., 2021). The self-attention mechanism enables capturing nuanced relationships in data. SwinU-Net integrates U-Net's contracting and expanding paths in decoding, emphasizing spatial detail preservation. This combination empowers SwinU-Net to excel in tasks requiring precise localization and robust contextual understanding.
7. *SegFormer*. SegFormer represents a significant advancement in semantic segmentation by leveraging a transformer-based architecture (Xie et al., 2021). Unlike traditional CNN approaches, SegFormer employs a hierarchical transformer encoder to capture multi-scale contextual information effectively without relying on complex designs such as positional encodings or large pre-training datasets. The decoder in SegFormer integrates features from different scales using lightweight multi-layer perceptron, ensuring efficient and precise segmentation. This innovative design enables SegFormer to achieve excellent segmentation results with medium-sized parameters and fast inference speed in high-resolution complex scenes.

4.2 Loss function and accuracy evaluation

Since the landslide detection is a two-class semantic segmentation task, we choose the binary cross-entropy (De Boer et al., 2005) as the loss function for model training, whose mathematical expression is as follows:

$$L(y, \hat{y}) = -\frac{1}{N} \sum_{i=1}^N [y_i \log(\hat{y}_i) + (1 - y_i) \log(1 - \hat{y}_i)], \quad (1)$$

where L is the loss function, N is the number of samples, y_i is the true label (0 or 1) of the i th sample, and \hat{y}_i is the predicted probability of the i th sample.

For accuracy evaluation, the following accuracy indicators are calculated through confusion matrices (Townsend, 1971): precision, recall, F_1 score (Chicco and Jurman, 2020), and mean intersection over union (mIoU) (Rezatofighi et al., 2019). Their calculation formulas are as follows:

$$\text{precision} = \frac{\text{TP}}{\text{TP} + \text{FP}}, \quad (2)$$

$$\text{recall} = \frac{\text{TP}}{\text{TP} + \text{FN}}, \quad (3)$$

$$F_1 = \frac{2 \times \text{precision} \times \text{recall}}{\text{precision} + \text{recall}}, \quad (4)$$

$$\text{mIoU} = \frac{1}{N} \sum_{i=1}^N \frac{\text{TP}_i}{\text{TP}_i + \text{FP}_i + \text{FN}_i}, \quad (5)$$

where TP is the true positive, FP is the false positive, TN is the true negative, and FN is the false negative.

4.3 Equipment and parameter

The deep learning framework employed in this study is conducted based on PaddlePaddle 2.3.2 (Ma et al., 2019), with the environment configured for Python 3.8, CUDA 11.2, and CuDNN 8.3.0. The experimental setup encompasses an Intel Xeon CPU, W2255, 3.7 GHz, equipped with 256 GB of system memory. The GPU infrastructure consists of a Tesla V100, with 32 GB of video memory. The operating system employed is Ubuntu 20.04. The model's optimizer is selected as AdamW (Loshchilov and Hutter, 2017), with an initial learning rate of 0.0006 and beta1 is set to 0.9, beta2 to 0.999, weight decay to 0.01, and epoch to 100.

5 Results

To validate the accuracy of the GDCLD dataset, this study selected four types of remote sensing images (UAV, PlanetScope, Map World, and Gaofen-6) from five seismic events (Luding, Jiuzhaigou, Hokkaido, Mainling, and Nippes) as training and validation datasets for model construction and accuracy evaluation. The ratio of the training dataset to the validation dataset is 3 : 1. To further assess the generalization ability of this dataset, we chose three types of remote sensing images (UAV, PlanetScope, and Map World images) from

four independent seismic events (Lushan, Mesetas, Sumatra, and Palu) as the test dataset. Considering the geographical distribution, these four regions, located on different continents and characterized by distinct tectonic settings and climatic conditions, ensure complete independence from the training dataset. From the perspective of data sources, the four study areas represent three major types of remote sensing imagery: PlanetScope, UAV, and Map World. Additionally, the UAV sensor used in the Lushan area is different from those used in other regions. This data partitioning strategy is designed to rigorously evaluate the generalization capability of the GDCLD-trained model.

We conducted evaluations on our dataset utilizing the aforementioned seven semantic segmentation algorithms. After each model is trained for 100 epochs, we meticulously examine the performance of the GDCLD dataset in landslide identification. We present the performance of the seven algorithms on the validation dataset in Table 4.

Among these seven algorithms, U-Net, ResU-Net, DeepLabV3, and HRNet serve as neural network models with convolutional structures, whereas UPerNet, SwinU-Net, and SegFormer are based on transformer-based neural network architectures. From Table 4, it is evident that transformer-based semantic segmentation models exhibit superior performance compared to models based on convolutional structures. Overall, the mIoU of the seven algorithms of the GDCLD validation set spans from 71.07 % to 85.06 %. Notably, U-Net demonstrates the lowest level of detection, with the mIoU and F_1 score of 71.07 % and 79.54 %. In contrast, SegFormer yields the best performance, with an accuracy of 91.35 %, recall of 91.70 %, F_1 score of 91.52 %, and mIoU of 85.06 %. Figure 6 illustrates the detection results of different models across various remote sensing data sources. It can be seen that transformer-based semantic segmentation models achieve superior segmentation outcomes.

To demonstrate the robustness and generalization capability of the dataset-trained models in other environment, we conducted testing using four independent events, as illustrated in Table 5. Overall, the mIoU performance of the algorithms trained on GDCLD ranges from 56.09 % to 72.84 %. SegFormer exhibits the best performance, achieving precision of 77.09 %, recall of 87.09 %, F_1 score of 81.88 %, and mIoU of 72.84 %. We present detailed results of six types of remote sensing images in these four events in Table 6. The overall mIoU ranges from 69.01 % to 82.31 %, while the F_1 ranges from 80.63 % to 89.30 %. Furthermore, we noticed a remarkable imbalance between recall and precision in the predicted results. The recall is always higher than the precision as it is crucial to not miss any important landslides for disaster assessment and rescue operations. From the perspective of remote sensors, except for the Sumatra incident, higher resolution was directly related to better landslide detection performance.

Figures 7 to 10, respectively, illustrate the detection results for Mesetas (PlanetScope), Sumatra (PlanetScope),

Palu (Map World), and Lushan (UAV). The F_1 score of the Mesetas event model is 80.63 %, with recall and precision exhibiting relative balance. As observed in Fig. 7, our model demonstrates strong capabilities in detecting and segmenting the majority of landslides, particularly in regions of mountainous slopes (Fig. 7d). In areas affected by mountain shadows (Fig. 7b, c, and e), this is as expected since pixel signatures of shadows are very different than those of landslides. While the model successfully identifies the majority of landslide pixels, it displays some omissions, particularly in portions of the landslides that are obscured by shadows. Additionally, smaller landslides in these shadowed areas are occasionally entirely missed. In the Sumatra event, we attained remarkably excellent detection results, with an F_1 score of 89.30 %, recall of 97.45 %, and precision of 83.57 %; recall is 13.88 % higher than precision. As illustrated in Fig. 8, the model effectively identifies nearly all landslides (Fig. 8b and c). However, there are instances of missed landslide detection in the lower-right corner of Fig. 8a. This is due to the apparent confusion between the landslide accumulation area and river channels, resulting in sub-optimal detection. In the Palu event, our F_1 score yielded a result of 81.40 %, with recall reaching 91.24 % and precision 73.48 %; recall is 17.76 % higher than precision. As depicted in Fig. 9, the detection outcomes effectively discriminate between numerous cloud obscuration, bare lands, and buildings, underscoring the positive efficacy of augmenting negative samples in our dataset to improve the model's detection capabilities. Similarly, for the Lushan event captured by UAV, we achieved an F_1 score of 81.80 %, with recall and precision values of 90.35 % and 74.72 %, respectively, and recall exceeding precision by 15.63 %. As shown in Fig. 10, in the UAV data, the model demonstrates exceptional segmentation capabilities for large-scale landslides (Fig. 10b, c, and d), while its detection performance for some small-scale disasters is less satisfactory. Overall, the model trained based on GDCLD demonstrated excellent generalization capabilities across four independent test datasets. It successfully detected all major landslides and effectively segmented landslide boundaries. More importantly, the model effectively excluded background noise from the river channels, bare ground in residential areas, and cloud region, showcasing its remarkable robustness.

6 Discussion

6.1 Sample richness of GDCLD

The GDCLD dataset stands out as the most extensive and comprehensive repository of landslide data currently available, encompassing landslide data from various geographic environments and multiple remote sensing sources. The annotated landslide labels within this dataset tally up to approximately 1.39×10^9 pixels, roughly 6 times as many annotations as all the other publicly accessible landslide datasets (Fig. 11). Additionally, this dataset includes a variety of neg-

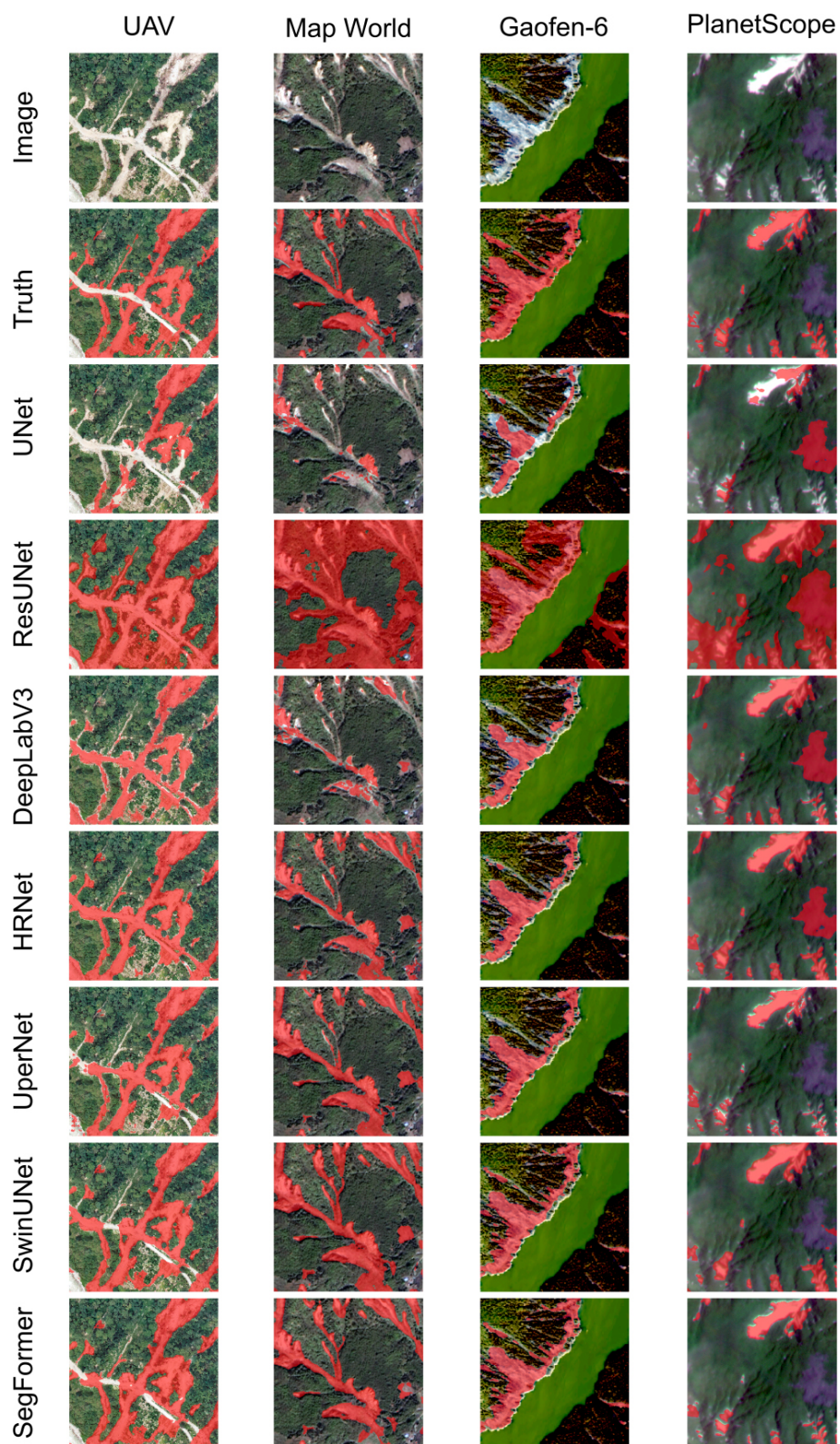


Figure 6. Comparative results of different algorithms using the validation dataset.

Table 4. Comparison of results with the GDCLD validation dataset. The highest scores are highlighted in bold.

Method	Backbone	Precision [%]	Recall [%]	F_1 [%]	mIoU [%]
U-Net	–	77.05	82.01	79.54	71.07
ResU-Net	ResNet-50	78.17	86.48	82.11	71.94
DeepLabV3	ResNet-50	81.27	86.96	84.02	74.61
HRNet	HRNet-48	81.88	87.21	84.46	75.19
UPerNet	ViT-B16	88.18	90.64	89.39	81.97
SwinU-Net	–	89.78	92.01	90.72	83.68
SegFormer	MiT-B4	91.35	91.70	91.52	85.06

Table 5. Comparison of results with the test dataset. The highest scores are highlighted in bold.

Method	Backbone	Precision [%]	Recall [%]	F_1 [%]	mIoU [%]
U-Net	–	61.69	61.22	61.45	56.09
ResU-Net	ResNet-50	66.56	64.46	65.49	57.06
DeepLabV3	ResNet-50	65.26	67.75	66.48	59.73
HRNet	HRNet-48	65.52	72.03	68.62	61.79
UPerNet	ViT-B16	69.96	78.08	73.80	65.42
SwinU-Net	–	71.56	82.26	76.54	67.18
SegFormer	MiT-B4	77.09	87.09	81.88	72.84

ative samples with optical characteristics similar to landslides, which can significantly enhance the model's generalization capability. In contrast to other datasets, which are limited to training small-scale semantic segmentation models like U-Net and DeepLabV3 (Xu et al., 2024; Meena et al., 2023; Ghorbanzadeh et al., 2022), the GDCLD dataset can effectively train large-scale semantic segmentation models such as transformers. Moreover, unlike Sentinel-2 and Landsat satellite imagery, where moderate spatial resolutions can limit the accurate delineation of landslide boundaries, GDCLD provides remarkably high spatial resolutions (0.2–3 m) and diverse spectral characteristics. This dataset not only performs well in landslide mapping across diverse geographical settings, but also serves as a baseline dataset for transfer learning in landslide detection.

6.2 Enhancement in model generalization

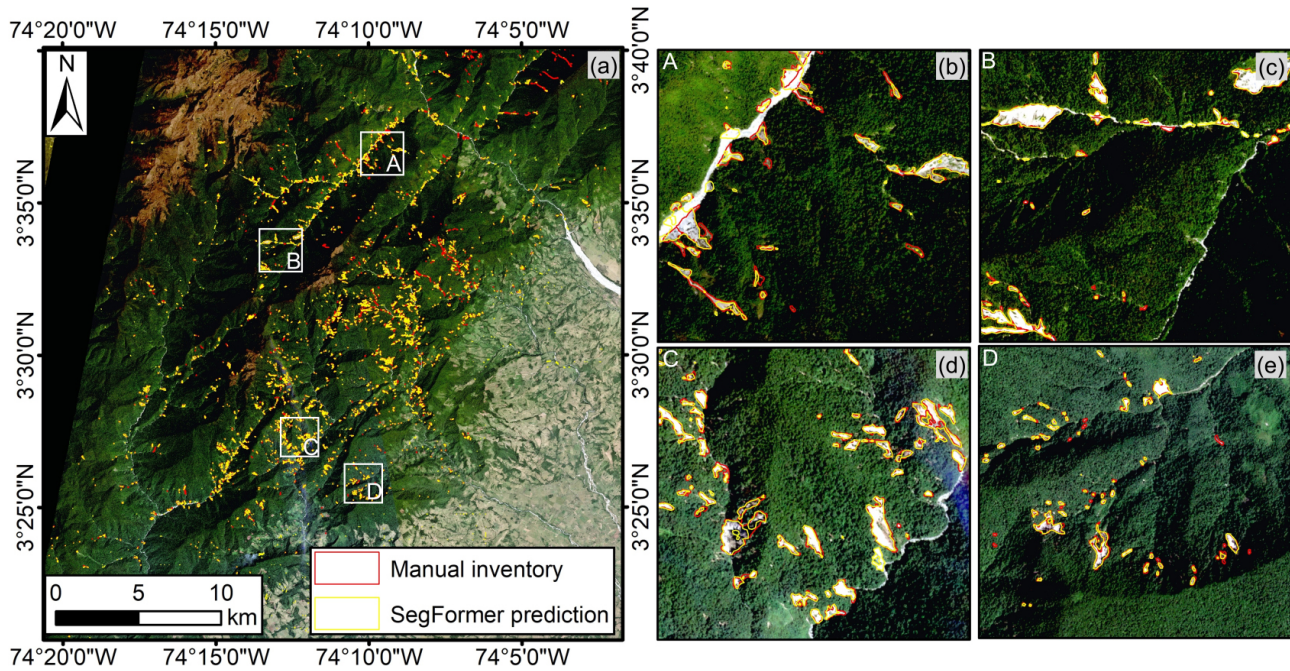
In the GDCLD dataset, a general selection of remote sensing data from multiple sources enhances the overall generalization capability of the landslide identification model. To substantiate this assertion, we conduct a comparative analysis between models trained by single- and multi-source datasets. The datasets from different sensors are segregated, and the SegFormer, which is an advanced and widely used transformer-based algorithm, is applied to train the landslide models. Their performance was verified by their respective test dataset as well as an independent event of Lushan earthquake.

The accuracy metrics for the validation dataset are presented in Table 7. Across four remote sensing sources – Plan-

etScope, Gaofen-6, Map World, and UAV – models trained on single-source datasets consistently demonstrate higher performance on test samples, with mIoU indices surpassing those of multi-source datasets by 2.26 %, 1.63 %, 0.64 %, and 0.13 %, respectively. However, a noteworthy observation emerges when models are transferred to the independent Lushan earthquake case (Table 8). The model trained on the multi-source dataset achieves significantly enhanced performance compared to the model derived from the single-source counterpart. The mIoU of UAV-, Map World- and PlanetScope-based datasets is improved by 8.16 %, 7.95 %, and 0.09 %, respectively. As depicted in Fig. 12, the models trained by multi-source images exhibit higher recalls, accurate landslide boundaries, and robust resistance to interference. The yellow circle highlights the enhancements of models trained by multi-source images compared to single-source images. From the perspective of data sources, Map World contains different types of images (such as Gaofen and Jilin), encompassing a multitude of spectral responses across these sensors. The UAV imagery in the Lushan event utilizes the sensor different from those in the Luding and Jiuzhaigou event, resulting in noticeable spectrum differences in images. Consequently, compared to a single remote sensing source, the generalization capability of the models trained by multi-source images demonstrates a more pronounced improvement. In contrast, PlanetScope imagery, obtaining data from the same satellite sensors, exhibits smaller spectral variations in various images. As a result, models trained on both single- and multi-source datasets achieve similar performance. This highlights the importance of datasets with diverse images sources for enhanced model performance in landslide map-

Table 6. Detection results of SegFormer in different events.

Events	Image type	Precision [%]	Recall [%]	F_1 [%]	mIoU [%]
Lushan	UAV	74.72	90.35	81.80	72.96
	Map World	76.18	87.35	81.38	71.92
	PlanetScope	81.50	82.28	81.78	69.05
Palu	Map World	73.48	91.24	81.40	71.12
Mesetas	PlanetScope	80.26	80.97	80.63	69.01
Sumatra	PlanetScope	83.57	97.45	89.30	82.31

**Figure 7.** Mesetas PlanetScope dataset. (a) Regional aerial view. (b–e) Detection results of four magnified areas.

ping. This indicates that the utilization of multi-source remote sensing datasets enables the model to learn the spectral characteristics of the images from diverse sensors. Hence, the model trained by GDCLD possesses an enhanced generalization ability and robustness, enabling it to effectively perform landslide mapping in independent cases without prior knowledge.

6.3 Comparison with existing landslide datasets and models

To assess the robustness and generalization capabilities of the GDCLD dataset, we employ SegFormer trained on the GDCLD dataset (GDCLD-S model) to identify landslides within three distinct datasets: HR-GLDD, GVLM, and CAS Landslide. Initially, we standardize the data from these three datasets to 1024×1024 -pixel remote sensing tiles. Subsequently, utilizing the GDCLD-S model, we conduct landslide identification across all these datasets. Table 9 demon-

strates favorable performance of the model across these diverse datasets. For instance, in the HR-GLDD dataset, which shares similarities with the PlanetScope imagery in GDCLD, the model achieves an mIoU of 76.97 %, indicating a balance between precision and recall metrics. Similarly, when applied to the GVLM dataset, leveraging Map World imagery, our dataset exhibits robust predictive outcomes, resulting in a comprehensive mIoU of 70.07 %. Likewise, for the CAS Landslide dataset, GDCLD demonstrates strong generalization capabilities, yielding an outstanding comprehensive metric with $mIoU = 76.91 \%$ alongside balanced recall and precision metrics.

Although all landslide samples contained in GDCLD are induced by seismic activity, our model demonstrates good detection capabilities for rainfall-induced landslides. These two categories exhibit distinct spectral characteristics from their surrounding environments. Consequently, models trained on GDCLD exhibit proficient detection capabilities for rainfall-induced landslides. We present the identifi-

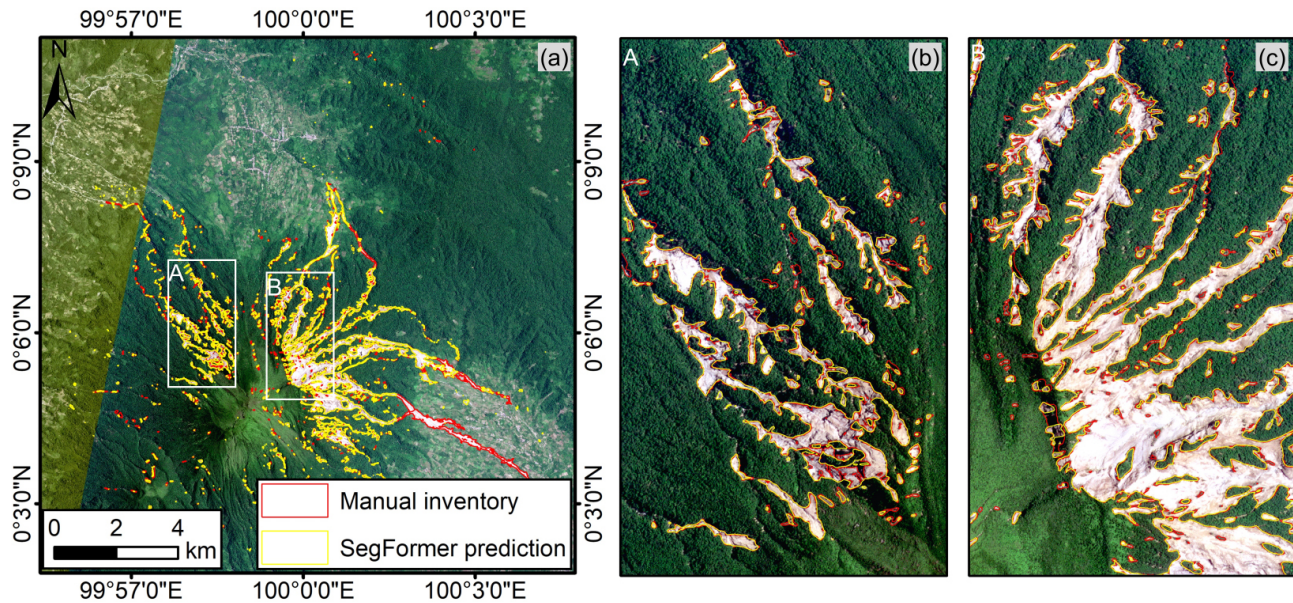


Figure 8. Sumatra PlanetScope dataset. (a) Regional aerial view. (b–c) Detection results of two magnified areas.

Table 7. GDCLD performances on validation dataset through single- and multi-source dataset. The highest scores are highlighted in bold.

Data source	Data type	Precision [%]	Recall [%]	F_1 [%]	mIoU [%]
Single source	UAV	92.20	92.90	92.54	87.07
	PlanetScope	87.98	87.81	87.89	80.11
	Map World	86.49	90.01	88.21	80.66
	Gaofen-6	91.25	88.04	89.62	83.61
Multiple sources	UAV	91.91	92.64	92.27	86.94
	PlanetScope	85.01	87.79	86.37	77.85
	Map World	86.42	89.12	87.74	80.02
	Gaofen-6	90.49	85.20	87.77	81.98

cation performance of a GDCLD-based model for rainfall-induced landslides from the GVLM dataset in Table 9 and Fig. 13. Figure 13 underscores the excellent detection performance of the GDCLD-S model on rainfall-induced landslides in the GVLM dataset. Despite occasional misclassifications of small-size targets, the model effectively delineates the majority of rain-induced landslides. The precision metrics in Table 8 affirm this observation with an mIoU reaching 78.22 % and both recall and precision exceeding 85 %. This highlights the robust generalization capability of the model trained by our dataset, enabling effective identification of rainfall-induced landslides.

In addition to the aforementioned analyses, we compare the performance of GDCLD with other two datasets, GVLM and CAS Landslide. Specifically, we train landslide detection models using the SegFormer algorithm on the GVLM and CAS Landslide datasets, denoted as GVLM-S and CAS-S, respectively, with identical training parameters as previously described. Furthermore, we also use DeepLabV3 to train the

CAS-D model based on the CAS Landslide dataset and use it for the comparison of landslide detection (Xu et al., 2024). Subsequently, the GDCLD-S, CAS-S, CAS-D, and GVLM-S models were applied to identify landslides in the Lushan area using three distinct remote sensing data sources: UAV, PlanetScope, and Map World. The results of this comparison are presented in Table 10. From Table 10, it is evident that the GDCLD-S model outperformed CAS-S, CAS-D, and GVLM-S across all three remote sensing datasets, achieving mIoU values of 72.96 %, 69.05 %, and 71.92 % for UAV, PlanetScope, and Map World, respectively. In contrast, CAS-S records mIoU values of 62.03 %, 56.86 %, and 60.35 % for the same datasets, respectively, which is better than the CAS-D model trained with DeepLabV3 and also illustrates the advantages of the transformer architecture over the CNN architecture. Notably, GDCLD-S exhibited a significantly higher recall than the other two models and also demonstrated an advantage in precision. Overall, GDCLD-S, along with CAS-S, exhibited superior performance compared to the single-

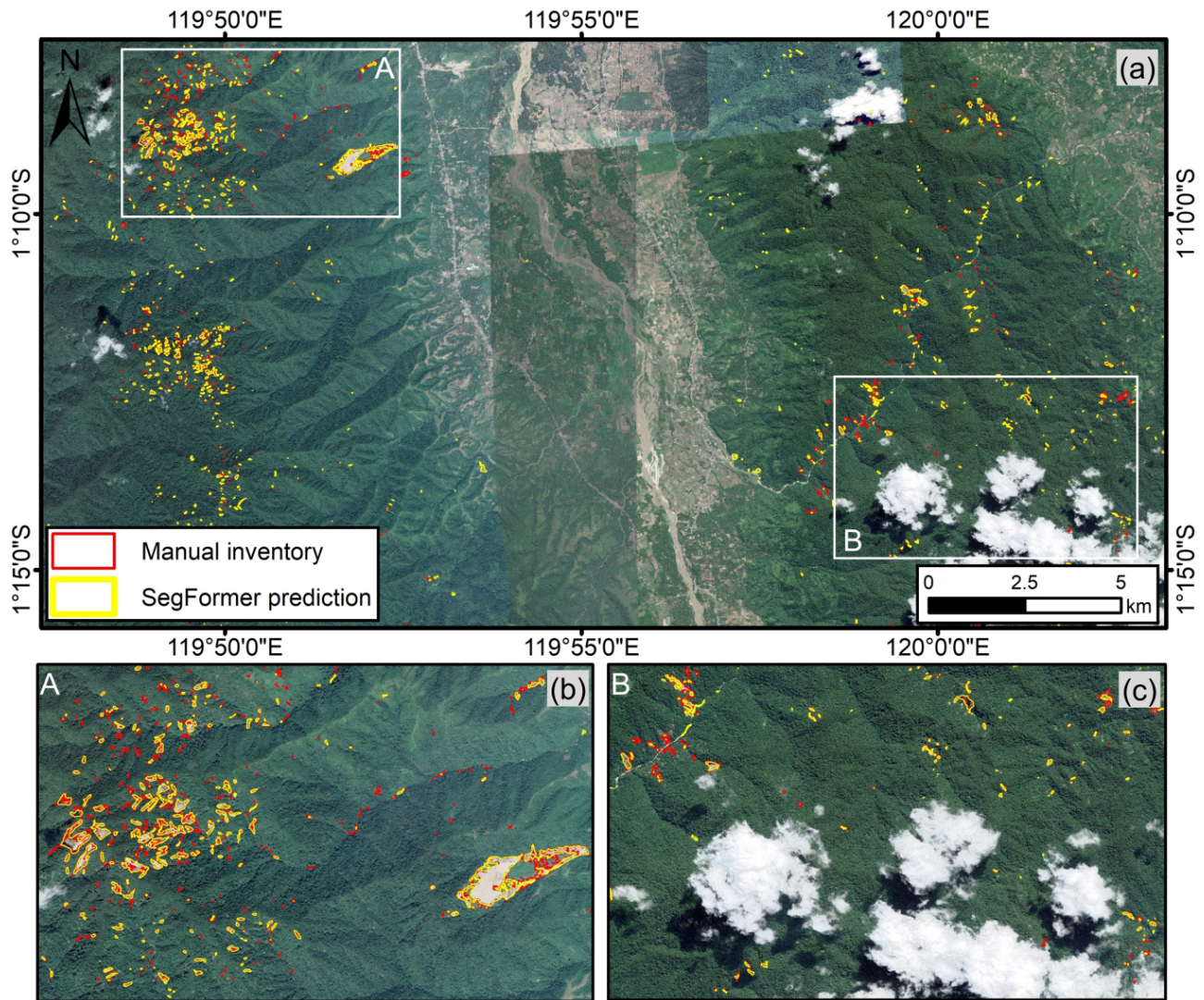


Figure 9. Palu Map World dataset. (a) Regional aerial view. (b–c) Detection results of two magnified areas.

Table 8. GDCLD performances on an unseen dataset through single- and multi-source dataset. The highest scores are highlighted in bold.

Data source	Data type	Precision [%]	Recall [%]	F_1 [%]	mIoU [%]
Single source	UAV	64.92	90.68	75.67	64.80
	PlanetScope	81.25	82.29	81.75	68.96
	Map World	68.39	80.16	73.81	63.97
Multiple sources	UAV	74.72	90.35	81.80	72.96
	PlanetScope	81.50	82.28	81.78	69.05
	Map World	76.18	87.35	81.38	71.92

source data model GVLM-S, particularly in handling multi-source remote sensing images. The extensive landslide data and negative samples included in GDCLD-S further contributed to its enhanced robustness against noise and improved recall in landslide detection.

6.4 Practical applications of GDCLD

To evaluate the practical applicability of the GDCLD, we selected two significant landslide-triggering events that occurred in April 2024 for rapid landslide identification. These events include landslides induced by heavy rainfall

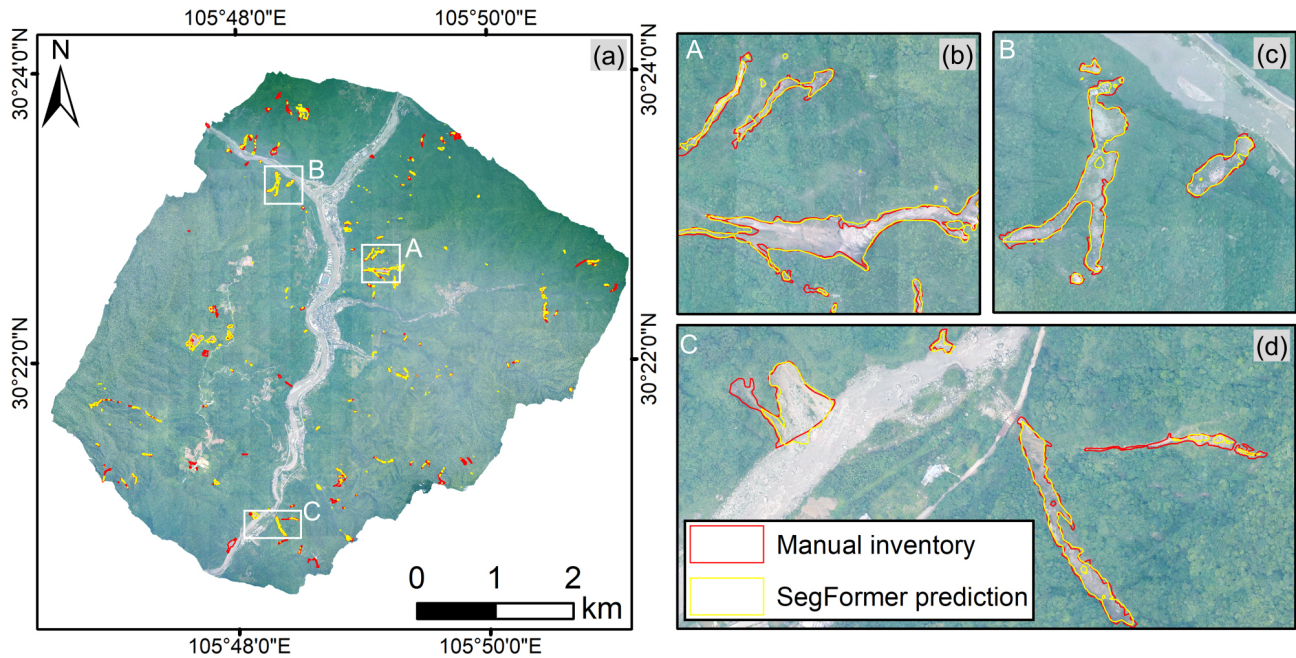


Figure 10. Lushan UAV dataset. (a) Regional aerial view. (b–d) Detection results of three magnified areas.

Table 9. Validation results of other public datasets.

Dataset	Precision [%]	Recall [%]	F_1 [%]	mIoU [%]
HR-GLDD	84.88	86.81	85.84	76.97
GVLM	72.83	87.54	80.68	70.07
CAS	82.95	86.35	84.62	76.91
GVLM rainfall	85.88	86.71	86.29	78.22

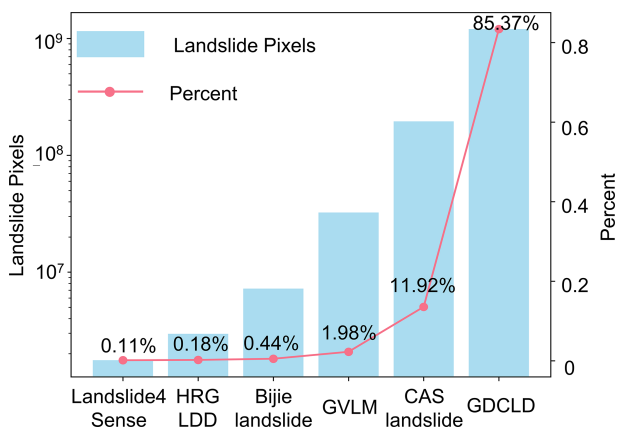


Figure 11. Statistical comparison of landslide pixels in different landslide datasets.

in Meizhou, China, and landslides triggered by an earthquake in Hualien, China. In both cases, PlanetScope imagery was employed for experimentation. For the Meizhou case, we obtained the image on 14 May 2024 and applied

the SegFormer model trained on GDCLD data to identify landslides triggered by heavy rainfall. The results, shown in Fig. 14, demonstrate that the GDCLD-trained model effectively mapped newly induced landslides with a total area of 8.49 km². The model exhibited excellent accuracy in avoiding false positives such as buildings, roads, and rivers. In terms of the Hualien event, we acquired post-event images from 17 to 29 April 2024. The rapid identification results, displayed in Fig. 15, indicate that the GDCLD-trained model effectively eliminates false positives such as roads, buildings, bare ground, and rivers, with an identified landslide area of 90.9 km². The original PlanetScope images and landslide recognitions of the two events are available at <https://doi.org/10.5281/zenodo.13612636> (Fang et al., 2024).

7 Future research directions

The current GDCLD primarily comprises landslide samples from regions with significant vegetation coverage, with limited representation from areas with low vegetation cover, such as loess landslides. To address this, we have updated the database with high-resolution UAV data (0.1 m resolu-

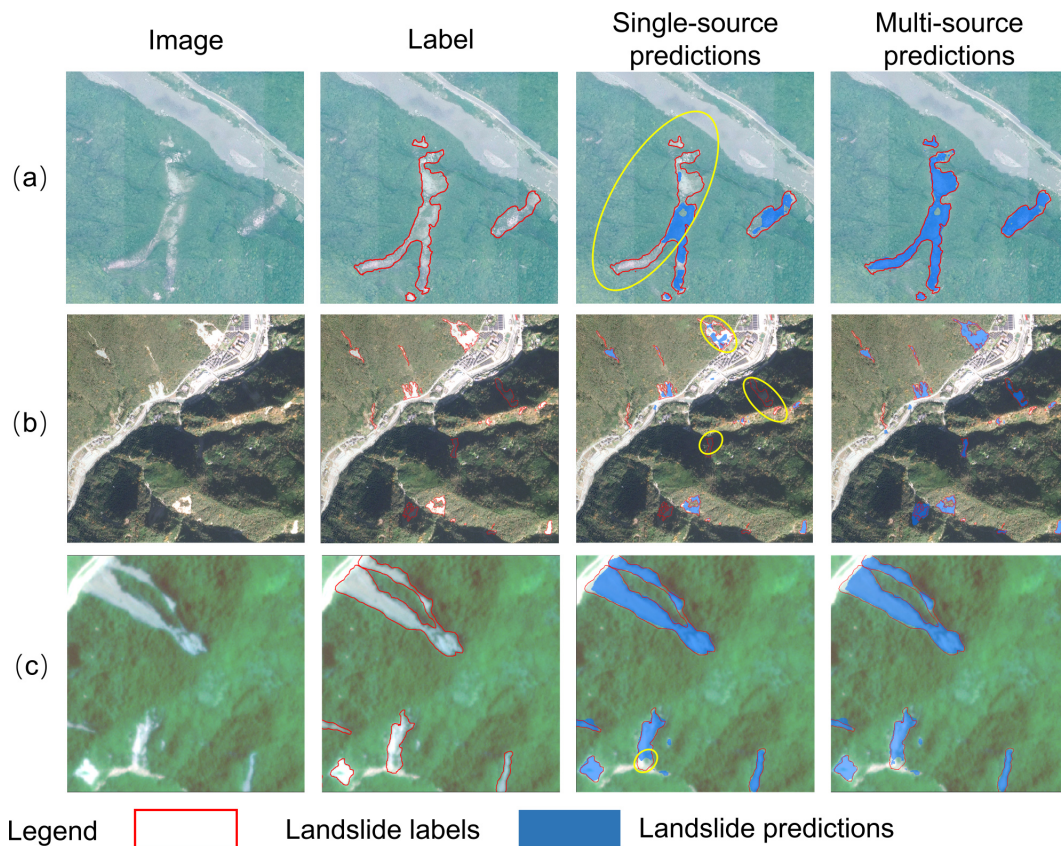


Figure 12. Comparison of the results of ablation experiments between multi- and single-source imagery of (a) UAV, (b) Map World, and (c) PlanetScope.

Table 10. Performance comparison of GDCLD-S, GVLM-S, CAS-S, and CAS-D using the Lushan dataset. The highest scores are highlighted in bold.

Model	Data type	Precision [%]	Recall [%]	F_1 [%]	mIoU [%]
CAS-D	UAV	72.73	55.34	62.88	57.91
	PlanetScope	52.07	56.05	53.93	52.86
	Map World	61.79	70.50	64.9	58.11
GVLM-S	UAV	73.03	54.84	57.67	53.41
	PlanetScope	60.13	53.40	54.82	51.52
	Map World	77.71	66.40	71.56	63.97
CAS-S	UAV	74.08	67.05	69.95	62.03
	PlanetScope	58.56	76.57	66.40	56.86
	Map World	75.02	64.65	68.37	60.35
GDCLD-S	UAV	74.72	90.35	81.80	72.96
	PlanetScope	81.50	82.28	81.78	69.05
	Map World	76.18	87.35	81.38	71.92

tion) of loess landslides triggered by the M_w 6.2 earthquake in Jishishan, Gansu, China, in December 2023 (Chen et al., 2024). Incorporating these loess landslide samples enhances the dataset's diversity and improves the generalization capability of landslide detection models. Ongoing efforts to track

and integrate data from landslides triggered by future extreme events, including strong earthquakes, heavy rainfall, and hurricanes, will further enrich the dataset.

In addition to expanding the GDCLD dataset, developing a large-scale vision model for landslide detection, such as a

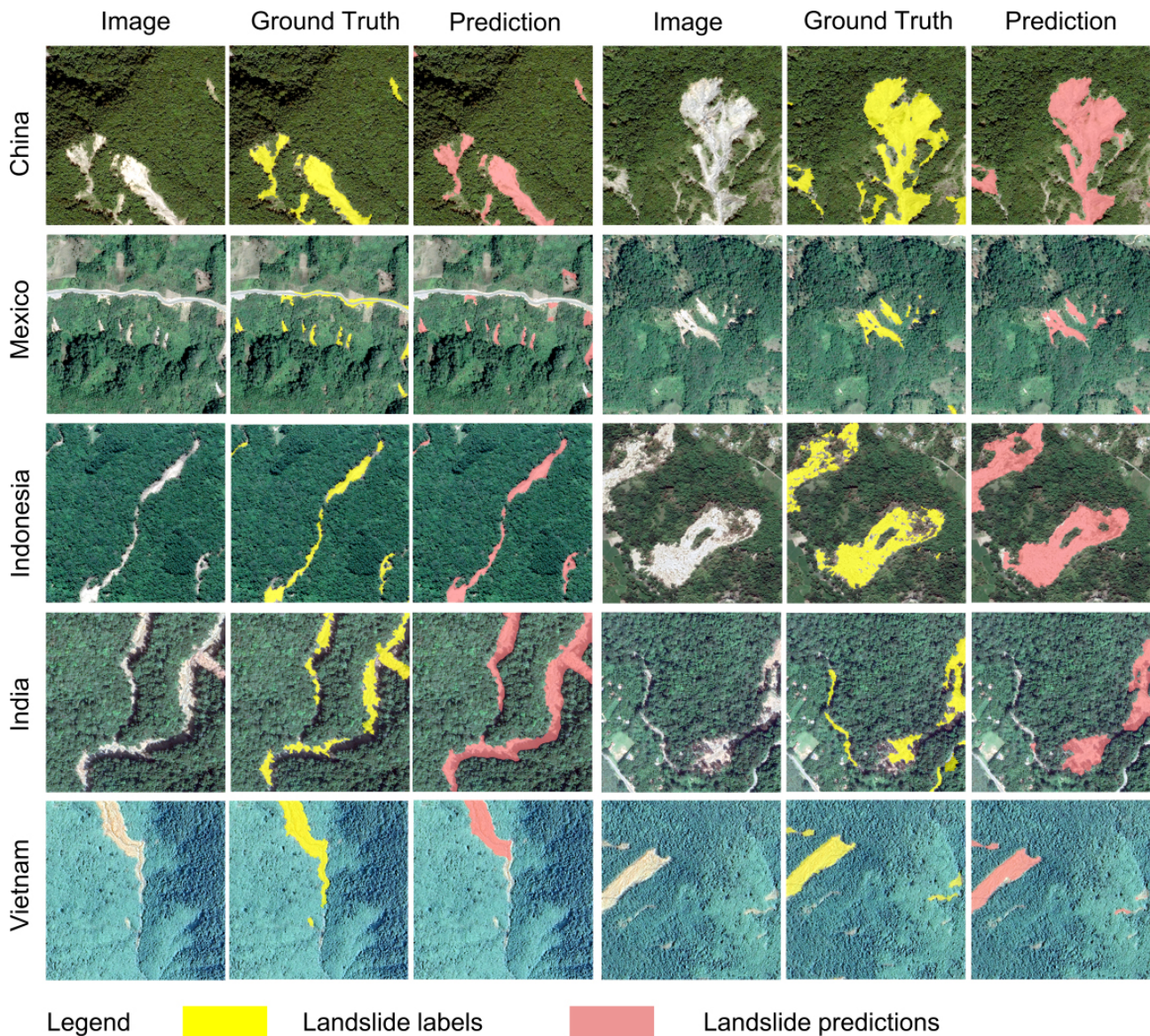


Figure 13. Detection results of rainfall landslides by the GDCLD-S model. Map credit: GVL.M.

Segment Anything Model tailored for landslide identification and trained on GDCLD, is a crucial step forward in advancing AI-based landslide detection. This model will be used for the intelligent recognition of landslides in multi-source remote sensing images on a global scale.

Note that GDCLD is generally more applicable to semantic segmentation rather than instance segmentation for the landslide identification task. Unlike other instance segmentation tasks, landslide segmentation presents unique challenges due to the frequent mixing of the “deposit” areas of adjacent landslide bodies (Hung et al., 2014). In most cases, we can only intuitively identify the “source” area of a landslide. This phenomenon is commonly observed in events such as the landslides triggered by the 2022 Luding earthquake in

China (Fig. S10). Under these circumstances, it is often not feasible to directly separate individual landslides from 2D optical images. Instead, it is necessary to consider the movement characteristics of each object from a 3D perspective (Bhuyan et al., 2024; Marc and Hovius, 2015) and combine this with topographic data to create accurate landslide labels, for instance, for segmentation. However, generating such datasets requires high-resolution digital elevation models (DEMs) and UAV or direct use of point cloud data. Given the global limitations in publicly available DEMs (30 m), achieving such fine distinctions is challenging. Therefore, our current study primarily focuses on semantic segmentation tasks. In future research, we plan to prepare landslide

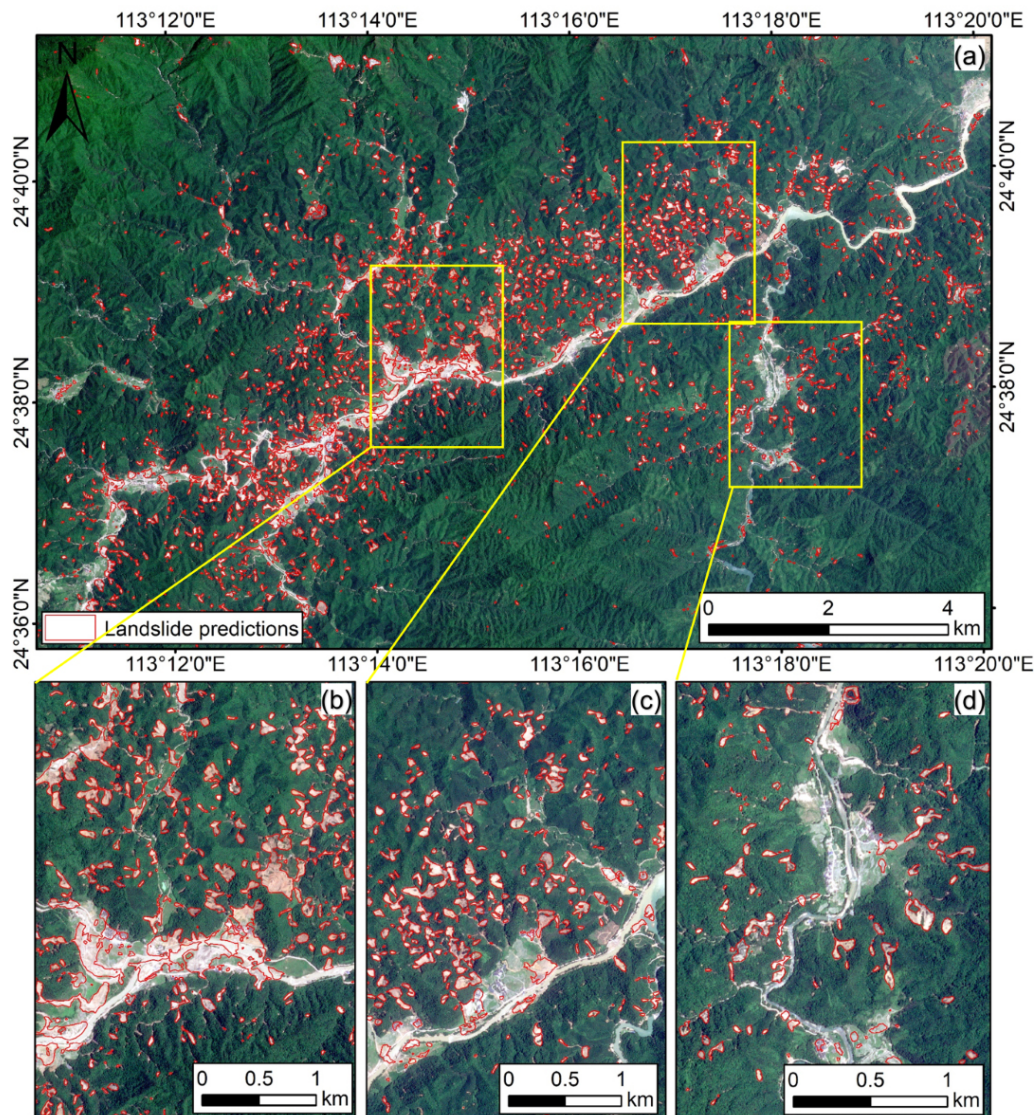


Figure 14. Detection results of rainfall-induced landslides for Meizhou, China. In panel (a) is the aerial view of the whole area, and in panels (b), (c), and (d) are the partial details. Map credit: PlanetScope.

labels and develop specialized algorithms for the landslide instance segmentation task based on a lidar dataset.

8 Code and data availability

The data are freely available at <https://doi.org/10.5281/zenodo.13612636> (Fang et al., 2024). The repository contains compressed folders – namely, `train_dataset.zip`, `val_dataset.zip`, and `test_dataset.zip`. The `train_dataset.zip` file contains 11 162 TIFF-format RGB images and their corresponding binary label data, each image with dimensions of 1024×1024 pixels. The `val_dataset.zip` file comprises 4459 TIFF-format RGB images and binary label data, with each image also sized at 1024×1024 pixels. The `test_data.zip` file includes seven original remote

sensing images from four landslide events, with images in TIFF-format RGB and labels in TIFF-format binary data, though the image dimensions vary. The “Future work” folder contains some remote sensing data that will be added later. For each label, 0 indicates the background, while 1 denotes a landslide. In addition, the other original data of UAV, Map World, and Gaofen-6 are non-public data. Both Map World and Gaofen-6 datasets were accessed under an image license acquired by our team. The UAV data are under the usage rights of the laboratory affiliated with our team. If you need to use them, please contact the corresponding author. The original PlanetScope data were obtained through the Planet Education and Research Program. You can get original imageries at <https://www.planet.com/> (Planet Team, 2019). The code used to produce data described in this paper

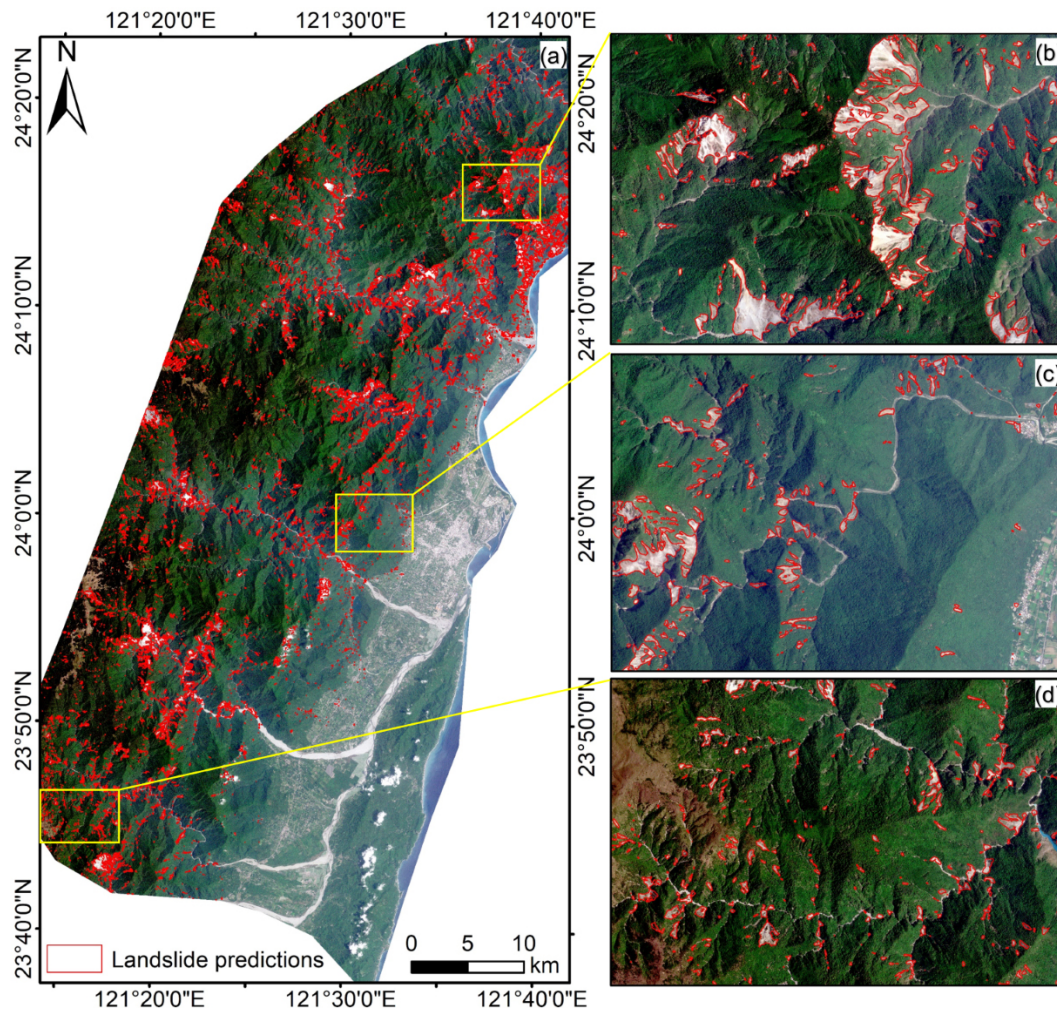


Figure 15. Detection results of earthquake-triggered landslides for Hualien, China. In panel (a) is the aerial view of the whole area, and in panels (b), (c), and (d) are the partial details. Map credit: PlanetScope.

as well as to create figures and tables can be accessed at <https://doi.org/10.5281/zenodo.13956757> (Fang, 2024).

9 Conclusion

Landslide mapping across extensive geographic areas using remote sensing has proven to be a significant challenge. Although previous attempts have produced landslide datasets and advanced automation and intelligence, they have not been able to overcome limitations of specific events and data sources. In this research, we proposed the Globally Distributed Coseismic Landslide Dataset (GDCLD), an innovative resource crafted to autonomously and precisely tackle the intricacies of landslide mapping. We made three significant contributions in this world. Firstly, we meticulously interpreted multi-source remote sensing data to create a comprehensive dataset for landslide detection. This dataset contains 1.39×10^9 annotated landslide pixels and remote sens-

ing images at four different resolutions spanning nine global regions. It successfully addresses the crucial lack of large-scale datasets in current landslide identification research. Secondly, we utilized a GDCLD-trained model to showcase its robustness and generalization in landslide identification across diverse geographical contexts. Our proposed dataset shows a great potential in the rapid response and emergency management of geological hazards. Although the landslide samples are obtained from seismic events, the trained model enables capturing and learning the characteristic differences between the landslides and the surroundings, making them suitable for landslide mapping beyond seismic-triggered events, such as those caused by rainfall. The comparative analyses with existing datasets highlight its effectiveness as the database of a deep learning model in mapping landslides across various global regions. Finally, we demonstrate the superiority of the transformer architecture over the conventional CNN architecture in the task of landslide iden-

tification using multi-source remote sensing imagery. The GDCLD-S model further highlights the enhanced generalization capabilities of multi-source data compared to single-source data. This work has great practical implications for the prevention and mitigation of geological hazards worldwide.

Supplement. The supplement related to this article is available online at: <https://doi.org/10.5194/essd-16-4817-2024-supplement>.

Author contributions. All the authors contributed equally to the preparation of the paper from data curation to the review of the final paper.

Competing interests. The contact author has declared that none of the authors has any competing interests.

Disclaimer. Publisher's note: Copernicus Publications remains neutral with regard to jurisdictional claims made in the text, published maps, institutional affiliations, or any other geographical representation in this paper. While Copernicus Publications makes every effort to include appropriate place names, the final responsibility lies with the authors.

Acknowledgements. The research is supported by the National Science Fund for Distinguished Young Scholars of China (grant no. 42125702), the National Natural Science Foundation of China (grant no. 42307263), the New Cornerstone Science Foundation through the Xplorer Prize (grant no. XPLOER-2022-1012), the Natural Science Foundation of Sichuan Province (grant nos. 24JBGS0060, 2022NSFSC0003, and 2022NSFSC1083), and the China Scholarship Council (CSC; grant no. 202409230002). We would like to thank the State Key Laboratory of Geohazard Prevention and Geoenvironment Protection for providing UAV data, the National Platform for Common GeoSpatial Information Services for Map World data, and the China Centre for Resources Satellite Data and Application for Gaofen-6 data. We would like to thank Kushanav Bhuyan for helping improve the quality of English and general writing in a previous version of this paper. We sincerely thank all colleagues who contributed to the landslide interpretation work. Finally, we sincerely thank the anonymous reviewers for their precious time and insightful comments, which were very helpful for us to improve the quality and readability of our paper.

Financial support. The research is supported by the National Science Fund for Distinguished Young Scholars of China (grant no. 42125702), the National Natural Science Foundation of China (grant no. 42307263), the New Cornerstone Science Foundation through the XPLOER PRIZE (grant no. XPLOER-2022-1012), the Natural Science Foundation of Sichuan Province (grant nos. 24JBGS0060, 2022NSFSC0003 and 2022NSFSC1083), and the China Scholarship Council (CSC; grant no. 202409230002).

Review statement. This paper was edited by Dalei Hao and reviewed by three anonymous referees.

References

- Alpert, L.: Rainfall maps of Hispaniola, *B. Am. Meteorol. Soc.*, 23, 423–431, 1942.
- Basofi, A., Fariza, A., and Dzulkarnain, M. R.: Landslides susceptibility mapping using fuzzy logic: A case study in Ponorogo, East Java, Indonesia, in: Proceedings of the 2016 International Conference on Data and Software Engineering (ICoDSE), Malang, Indonesia, pp. 1–7, <https://doi.org/10.1109/ICODSE.2016.7936156>, 2016.
- Bhuyan, K., Rana, K., Ferrer, J. V., Cotton, F., Ozturk, U., Catani, F., and Malik, N.: Landslide topology uncovers failure movements, *Nat. Commun.*, 15, 2633, <https://doi.org/10.1038/s41467-024-46741-7>, 2024.
- Bhuyan, K., Tanyaş, H., Nava, L., Puliero, S., Meena, S. R., Floris, M., Van Westen, C., and Catani, F.: Generating multi-temporal landslide inventories through a general deep transfer learning strategy using HR EO data, *Sci. Rep.*, 13, 162, <https://doi.org/10.1038/s41467-024-46741-7>, 2023.
- Brardinoni, F., Slaymaker, O., and Hassan, M. A.: Landslide inventory in a rugged forested watershed: a comparison between air-photo and field survey data, *Geomorphology*, 54, 179–196, 2003.
- Burrows, K., Walters, R. J., Milledge, D., Spaans, K., and Densmore, A. L.: A new method for large-scale landslide classification from satellite radar, *Remote Sens.-Basel*, 11, 237, <https://doi.org/10.3390/rs11030237>, 2019.
- Calais, E., Symithe, S., Monfret, T., Delouis, B., Lomax, A., Courboux, F., Ampuero, J. P., Lara, P. E., Bletery, Q., Cheze, J., Peix, F., Deschamps, A., de Lpinay, B., Raimbault, B., Jolivet, R., Paul, S., St Fleur, S., Boisson, D., Fukushima, Y., Duputel, Z., Xu, L., and Meng, L.: Citizen seismology helps decipher the 2021 Haiti earthquake, *Science*, 376, 283–287, <https://doi.org/10.1126/science.abn1045>, 2022.
- Cao, H., Wang, Y., Chen, J., Jiang, D., Zhang, X., Tian, Q., and Wang, M.: Swin-UNET: UNet-like pure transformer for medical image segmentation, in: Proceedings of the European Conference on Computer Vision (ECCV 2022 Workshops), Tel Aviv, Israel, 23–28 October 2022, pp. 9, https://doi.org/10.1007/978-3-031-25066-8_9, 2022.
- Casagli, N., Intrieri, E., Tofani, V., Gigli, G., and Raspini, F.: Landslide detection, monitoring and prediction with remote-sensing techniques, *Nat. Rev. Earth Environ.*, 4, 51–64, 2023.
- Chau, K. T., Sze, Y., Fung, M., Wong, W., Fong, E., and Chan, L.: Landslide hazard analysis for Hong Kong using landslide inventory and GIS, *Comput. Geosci.*, 30, 429–443, 2004.
- Chen, B., Xu, B., Zhu, Z., Yuan, C., Suen, H. P., Guo, J., Xu, N., Li, W., Zhao, Y., and Yang, J.: Stable classification with limited sample: Transferring a 30-m resolution sample set collected in 2015 to mapping 10-m resolution global land cover in 2017, *Sci. Bull.*, 64, 3, <https://doi.org/10.1016/j.scib.2019.03.002>, 2019.
- Chen, D., Yuan, R., Wang, P., Tian, Y., Hu, G., An, J., and Ma, S.: Preliminary study on the development characteristics and formation mechanism of the Zhongchuan Town liquefaction landslide-mudflow-blockage disaster chain induced by the 2023 Jishis-

- han Earthquake in Gansu Province, *Landslides*, 21, 2467–2480, <https://doi.org/10.1007/s10346-024-02307-8>, 2024.
- Chen, L. C., Zhu, Y., Papandreou, G., Schroff, F., and Adam, H.: Encoder-Decoder with Atrous Separable Convolution for Semantic Image Segmentation, in: *Proceedings of the European Conference on Computer Vision (ECCV 2018)*, Munich, Germany, 8–14 September 2018, pp. 49, https://doi.org/10.1007/978-3-030-01234-2_49, 2018.
- Chicco, D. and Jurman, G.: The advantages of the Matthews correlation coefficient (MCC) over F1 score and accuracy in binary classification evaluation, *BMC Genomics*, 21, 6, <https://doi.org/10.1186/s12864-019-6413-7>, 2020.
- Cigna, F., Osmanoglu, B., Cabral-Cano, E., Dixon, T. H., Ávila-Olivera, J. A., Garduño-Monroy, V. H., DeMets, C., and Wdowinski, S.: Monitoring land subsidence and its induced geological hazard with Synthetic Aperture Radar Interferometry: A case study in Morelia, Mexico, *Remote Sens. Environ.*, 117, 146–161, 2012.
- Cigna, F., Tapete, D., and Lee, K.: Geological hazards in the UNESCO World Heritage sites of the UK: From the global to the local scale perspective, *Earth-Sci. Rev.*, 176, 166–194, 2018.
- Coe, J. A., Ellis, W. L., Godt, J. W., Savage, W. Z., Savage, J. E., Michael, J., Kibler, J. D., Powers, P. S., Lidke, D. J., and Debray, S.: Seasonal movement of the Slumgullion landslide determined from Global Positioning System surveys and field instrumentation, July 1998–March 2002, *Eng. Geol.*, 68, 67–101, 2003.
- Dai, L., Fan, X., Wang, X., Fang, C., Zou, C., Tang, X., Wei, Z., Xia, M., Wang, D., and Xu, Q.: Coseismic landslides triggered by the 2022 Luding Ms6. 8 earthquake, China, *Landslides*, 20, 1277–1292, 2023.
- De Boer, P.-T., Kroese, D. P., Mannor, S., and Rubinstein, R. Y.: A tutorial on the cross-entropy method, *Ann. Oper. Res.*, 134, 19–67, 2005.
- Diakogiannis, F. I., Waldner, F., Caccetta, P., and Wu, C.: ResUNet-a: A deep learning framework for semantic segmentation of remotely sensed data, *ISPRS J. Photogramm. Remote*, 162, 94–114, 2020.
- Fan, X., Scaringi, G., Xu, Q., Zhan, W., Dai, L., Li, Y., Pei, X., Yang, Q., and Huang, R.: Coseismic landslides triggered by the 8th August 2017 M_s 7.0 Jiuzhaigou earthquake (Sichuan, China): factors controlling their spatial distribution and implications for the seismogenic blind fault identification, *Landslides*, 15, 967–983, 2018.
- Fang, C.: GDCLD: A globally distributed dataset of coseismic landslide mapping via multi-source high-resolution remote sensing images (the code), Zenodo [code], <https://doi.org/10.5281/zenodo.13956757>, 2024.
- Fang, C., Fan, X., Zhong, H., Lombardo, L., Tanyas, H., and Wang, X.: A Novel historical landslide detection approach based on LiDAR and lightweight attention U-Net, *Remote Sens.-Basel*, 14, 4357, <https://doi.org/10.3390/rs14174357>, 2022.
- Fang, C., Fan, X., and Wang, X.: GDCLD: A globally distributed dataset of coseismic landslide mapping via multi-source high-resolution remote sensing images, Zenodo [data set], <https://doi.org/10.5281/zenodo.13612636>, 2024.
- Fiorucci, F., Cardinali, M., Carlà, R., Rossi, M., Mondini, A., Santurri, L., Ardizzone, F., and Guzzetti, F.: Seasonal landslide mapping and estimation of landslide mobilization rates using aerial and satellite images, *Geomorphology*, 129, 59–70, 2011.
- Fiorucci, F., Ardizzone, F., Mondini, A. C., Viero, A., and Guzzetti, F.: Visual interpretation of stereoscopic NDVI satellite images to map rainfall-induced landslides, *Landslides*, 16, 165–174, 2019.
- Gao, H., Yin, Y., Li, B., Gao, Y., Zhang, T., Liu, X., and Wan, J.: Geomorphic evolution of the Sedongpu Basin after catastrophic ice and rock avalanches triggered by the 2017 M_s 6.9 Milin earthquake in the Yarlung Zangbo River area, China, *Landslides*, 1–15, 2023.
- Gao, J. and Maro, J.: Topographic controls on evolution of shallow landslides in pastoral Wairarapa, New Zealand, 1979–2003, *Geomorphology*, 114, 373–381, 2010.
- Ghorbanzadeh, O., Xu, Y., Zhao, H., Wang, J., Zhong, Y., Zhao, D., Zang, Q., Wang, S., Zhang, F., and Shi, Y.: The outcome of the 2022 landslide4sense competition: Advanced landslide detection from multisource satellite imagery, *IEEE J. Sel. Top. Appl. Earth Obs.*, 15, 9927–9942, 2022.
- Gorum, T., Fan, X., van Westen, C. J., Huang, R. Q., Xu, Q., Tang, C., and Wang, G.: Distribution pattern of earthquake-induced landslides triggered by the 12 May 2008 Wenchuan earthquake, *Geomorphology*, 133, 152–167, 2011.
- Guzzetti, F., Mondini, A. C., Cardinali, M., Fiorucci, F., Santangelo, M., and Chang, K.-T.: Landslide inventory maps: New tools for an old problem, *Earth-Sci. Rev.*, 112, 42–66, 2012.
- Harp, E. L., Jibson, R. W., and Schmitt, R. G.: Map of landslides triggered by the January 12, 2010, Haiti earthquake, Reston, VA, Report 3353, USGeological Survey Scientific Investigations Map, <https://doi.org/10.3133/sim3353>, 2016.
- He, K., Zhang, X., Ren, S., and Sun, J.: Deep Residual Learning for Image Recognition, in: *Proceedings of the IEEE Conference on Computer Vision and Pattern Recognition (CVPR)*, Las Vegas, NV, USA, 27 June–2 July 2016, pp. 770–778, <https://doi.org/10.1109/CVPR.2016.90>, 2016.
- Hu, K., Zhang, X., You, Y., Hu, X., Liu, W., and Li, Y.: Landslides and dammed lakes triggered by the 2017 M_s 6.9 Milin earthquake in the Tsangpo gorge, *Landslides*, 16, 993–1001, 2019.
- Huang, R. and Fan, X.: The landslide story, *Nat. Geosci.*, 6, 325–326, 2013.
- Huang, R., Pei, X., Fan, X., Zhang, W., Li, S., and Li, B.: The characteristics and failure mechanism of the largest landslide triggered by the Wenchuan earthquake, May 12, 2008, China, *Landslides*, 9, 131–142, 2012.
- Huang, Y., Xu, C., Zhang, X., Xue, C., and Wang, S.: An Updated Database and Spatial Distribution of Landslides Triggered by the Milin, Tibet M_w 6.4 Earthquake of 18 November 2017, *J. Earth Sci.*, 32, 1069–1078, 2021.
- Hungr, O., Leroueil, S., and Picarelli, L.: The Varnes classification of landslide types, an update, *Landslides*, 11, 167–194, 2014.
- Ji, S., Yu, D., Shen, C., Li, W., and Xu, Q.: Landslide detection from an open satellite imagery and digital elevation model dataset using attention boosted convolutional neural networks, *Landslides*, 17, 1337–1352, 2020.
- Li, Z., Shi, W., Lu, P., Yan, L., Wang, Q., and Miao, Z.: Landslide mapping from aerial photographs using change detection-based Markov random field, *Remote Sens. Environ.*, 187, 76–90, 2016.
- Li, Z., Shi, A., Li, X., Dou, J., Li, S., Chen, T., and Chen, T.: Deep learning-based landslide recognition incorporating deformation characteristics, *Remote Sens.-Basel*, 16, 992, <https://doi.org/10.3390/rs16060992>, 2024.

- Liu, J., Huang, X., Song, G., Li, H., and Liu, Y.: Uninet: Unified architecture search with convolution, transformer, and MLP, in: Proceedings of the European Conference on Computer Vision (ECCV), Tel Aviv, Israel, 23–28 October 2022, pp. 33–49, https://doi.org/10.1007/978-3-031-19803-8_3, 2022.
- Liu, Z., Lin, Y., Cao, Y., Hu, H., Wei, Y., Zhang, Z., Lin, S., and Guo, B.: Swin transformer: Hierarchical vision transformer using shifted windows, in: Proceedings of the IEEE/CVF International Conference on Computer Vision (ICCV), Montreal, QC, Canada, 9–16 October 2021, pp. 9992–10002, <https://doi.org/10.1109/ICCV48922.2021.00986>, 2021.
- Loshchilov, I. and Hutter, F.: Decoupled weight decay regularization, arXiv [preprint], arXiv:1711.05101, <https://doi.org/10.48550/arXiv.1711.05101>, 2017.
- Lu, P., Qin, Y., Li, Z., Mondini, A. C., and Casagli, N.: Landslide mapping from multi-sensor data through improved change detection-based Markov random field, *Remote Sens. Environ.*, 231, 111235, <https://doi.org/10.1016/j.rse.2019.111235>, 2019.
- Luppino, L. T., Hansen, M. A., Kampffmeyer, M., Bianchi, F. M., Moser, G., Jenssen, R., and Anfinsen, S. N.: Code-Aligned Autoencoders for Unsupervised Change Detection in Multimodal Remote Sensing Images, *IEEE Trans. Neural Netw. Learn. Syst.*, 35, 60–72, <https://doi.org/10.1109/TNNLS.2022.3172183>, 2022.
- Ma, Y., Yu, D., Wu, T., and Wang, H.: PaddlePaddle: An open-source deep learning platform from industrial practice, *Front. Data Comput.*, 1, 105–115, 2019.
- Marc, O. and Hovius, N.: Amalgamation in landslide maps: effects and automatic detection, *Nat. Hazards Earth Syst. Sci.*, 15, 723–733, <https://doi.org/10.5194/nhess-15-723-2015>, 2015.
- Meena, S. R., Ghorbanzadeh, O., van Westen, C. J., Nachappa, T. G., Blaschke, T., Singh, R. P., and Sarkar, R.: Rapid mapping of landslides in the Western Ghats (India) triggered by 2018 extreme monsoon rainfall using a deep learning approach, *Landslides*, 18, 1937–1950, 2021.
- Meena, S. R., Nava, L., Bhuyan, K., Puliero, S., Soares, L. P., Dias, H. C., Floris, M., and Catani, F.: HR-GLDD: a globally distributed dataset using generalized deep learning (DL) for rapid landslide mapping on high-resolution (HR) satellite imagery, *Earth Syst. Sci. Data*, 15, 3283–3298, <https://doi.org/10.5194/essd-15-3283-2023>, 2023.
- Metternicht, G., Hurni, L., and Gogu, R.: Remote sensing of landslides: An analysis of the potential contribution to geo-spatial systems for hazard assessment in mountainous environments, *Remote Sens. Environ.*, 98, 284–303, 2005.
- Mohan, A., Singh, A. K., Kumar, B., and Dwivedi, R.: Review on remote sensing methods for landslide detection using machine and deep learning, *T. Emerg. Telecommun. T.*, 32, e3998, <https://doi.org/10.1002/ett.3998>, 2021.
- Mondini, A. C., Guzzetti, F., Chang, K.-T., Monserrat, O., Martha, T. R., and Manconi, A.: Landslide failures detection and mapping using Synthetic Aperture Radar: Past, present and future, *Earth-Sci. Rev.*, 216, 103574, <https://doi.org/10.1016/j.earscirev.2021.103574>, 2021.
- Nava, L., Monserrat, O., and Catani, F.: Improving landslide detection on SAR data through deep learning, *IEEE Geosci. Remote Sens. Lett.*, 19, 1–5, 2021.
- O’Shea, K. and Nash, R.: An introduction to convolutional neural networks, arXiv [preprint], arXiv:1511.08458, 2015.
- Planet Team: Education and RESEARCH: Satellite imagery solutions, Planet [data set], <https://www.planet.com/> (last access: 1 March 2024), 2019.
- Poveda, E., Pedraza, P., Velandia, F., Mayorga, E., Plicka, V., Gallovič, F., and Zahradník, J.: 2019 M_w 6.0 Mesetas (Colombia) Earthquake Sequence: Insights From Integrating Seismic and Morphostructural Observations, *Earth Space Sci.*, 9, e2022EA002465, <https://doi.org/10.1029/2022EA002465>, 2022.
- Rezatofghi, H., Tsoi, N., Gwak, J., Sadeghian, A., Reid, I., and Savarese, S.: Generalized Intersection Over Union: A Metric and a Loss for Bounding Box Regression, in: Proceedings of the IEEE/CVF Conference on Computer Vision and Pattern Recognition (CVPR), Long Beach, CA, USA, 16–21 June 2019, pp. 658–666, <https://doi.org/10.1109/CVPR.2019.00075>, 2019.
- Ronneberger, O., Fischer, P., and Brox, T.: U-net: Convolutional networks for biomedical image segmentation, *Medical Image Computing and Computer-Assisted Intervention – MICCAI 2015: 18th International Conference*, 5–9 October 2015, Munich, Germany, Proceedings, Part III 18, 234–241, 2015.
- Shao, X., Ma, S., and Xu, C.: Distribution and characteristics of shallow landslides triggered by the 2018 M_w 7.5 Palu earthquake, Indonesia, *Landslides*, 20, 157–175, 2023.
- Soares, L. P., Dias, H. C., Garcia, G. P. B., and Grohmann, C. H.: Landslide segmentation with deep learning: Evaluating model generalization in rainfall-induced landslides in Brazil, *Remote Sens.-Basel*, 14, 2237, <https://doi.org/10.3390/rs14092237>, 2022.
- Ss, V. C. and Shaji, E.: Landslide identification using machine learning techniques: Review, motivation, and future prospects, *Earth Sci. Inform.*, 15, 2063–2090, 2022.
- Tang, D., Ge, W., and Cao, X.: Stress triggering of the 2022 Lushan–Maerkang earthquake sequence by historical events and its implication for fault stress evolution in eastern Tibet, *Front. Earth Sci.*, 11, 1105394, <https://doi.org/10.3389/feart.2023.1105394>, 2023.
- Townsend, J. T.: Theoretical analysis of an alphabetic confusion matrix, *Perception & Psychophysics*, 9, 40–50, 1971.
- Udin, W. S., Norazami, N. A. S., Sulaiman, N., Che Zaudin, N. A., Ma’ail, S., and Mohamad Nor, A. N.: UAV Based Multi-spectral Imaging System for Mapping Landslide Risk Area Along Jeli-Gerik Highway, Jeli, Kelantan, in: Proceedings of the 2019 IEEE 15th International Colloquium on Signal Processing & Its Applications (CSPA), Penang, Malaysia, pp. 162–167, <https://doi.org/10.1109/CSPA.2019.8695995>, 2019.
- Valagussa, A., Marc, O., Frattini, P., and Crosta, G. B.: Seismic and geological controls on earthquake-induced landslide size, *Earth Planet. Sc. Lett.*, 506, 268–281, 2019.
- Wang, F., Fan, X., Yunus, A. P., Siva Subramanian, S., Alonso-Rodriguez, A., Dai, L., Xu, Q., and Huang, R.: Coseismic landslides triggered by the 2018 Hokkaido, Japan (M_w 6.6), earthquake: spatial distribution, controlling factors, and possible failure mechanism, *Landslides*, 16, 1551–1566, 2019.
- Wang, J., Sun, K., Cheng, T., Jiang, B., Deng, C., Zhao, Y., Liu, D., Mu, Y., Tan, M., and Wang, X.: Deep high-resolution representation learning for visual recognition, *IEEE T. Pattern Anal.*, 43, 3349–3364, 2020.
- Xiao, T., Liu, Y., Zhou, B., Jiang, Y., and Sun, J.: Unified Perceptual Parsing for Scene Understanding, in: *Computer Vision – ECCV 2018, European Conference on Com-*

- puter Vision, Munich, Germany, 8–14 September 2018, pp. 26, https://doi.org/10.1007/978-3-030-01228-1_26, 2018.
- Xie, E., Wang, W., Yu, Z., Anandkumar, A., Alvarez, J. M., and Luo, P.: SegFormer: Simple and efficient design for semantic segmentation with transformers, *Adv. Neur. In.*, 34, 12077–12090, 2021.
- Xu, Y., Ouyang, C., Xu, Q., Wang, D., Zhao, B., and Luo, Y.: CAS Landslide Dataset: A Large-Scale and Multisensor Dataset for Deep Learning-Based Landslide Detection, *Sci. Data*, 11, 12, <https://doi.org/10.1038/s41597-023-02847-z>, 2024.
- Yamagishi, H. and Yamazaki, F.: Landslides by the 2018 hokkaido iburi-tobu earthquake on september 6, *Landslides*, 15, 2521–2524, 2018.
- Yang, Z., Dai, D., Zhang, Y., Zhang, X., and Liu, J.: Rupture process and aftershock mechanisms of the 2022 Luding M6.8 earthquake in Sichuan, China, *Earthquake Science*, 35, 1–2, 2022a.
- Yang, Z., Xu, C., and Li, L.: Landslide detection based on ResU-net with transformer and CBAM embedded: two examples with geologically different environments, *Remote Sens.-Basel*, 14, 2885, <https://doi.org/10.3390/rs14122885>, 2022b.
- Ye, C., Li, Y., Cui, P., Liang, L., Pirasteh, S., Marcato, J., Goncalves, W. N., and Li, J.: Landslide detection of hyperspectral remote sensing data based on deep learning with constrains, *IEEE J. Sel. Top. Appl. Earth Obs.*, 12, 5047–5060, 2019.
- Yi, Y., Zhang, Z., Zhang, W., Jia, H., and Zhang, J.: Landslide susceptibility mapping using multiscale sampling strategy and convolutional neural network: A case study in Jiuzhaigou region, *Catena*, 195, 104851, <https://doi.org/10.1016/j.catena.2020.104851>, 2020.
- Zhang, X., Yu, W., Pun, M.-O., and Shi, W.: Cross-domain landslide mapping from large-scale remote sensing images using prototype-guided domain-aware progressive representation learning, *ISPRS J. Photogramm.*, 197, 1–17, 2023.
- Zhao, B., Li, W., Su, L., Wang, Y., and Wu, H.: Insights into the landslides triggered by the 2022 Lushan Ms 6.1 earthquake: spatial distribution and controls, *Remote Sens.-Basel*, 14, 4365, <https://doi.org/10.3390/rs14174365>, 2022a.
- Zhao, B., Wang, Y., Li, W., Lu, H., and Li, Z.: Evaluation of factors controlling the spatial and size distributions of landslides, 2021 Nippes earthquake, Haiti, *Geomorphology*, 415, 108419, <https://doi.org/10.1016/j.geomorph.2022.108419>, 2022b.
- Zhong, C., Liu, Y., Gao, P., Chen, W., Li, H., Hou, Y., Nuremanguli, T., and Ma, H.: Landslide mapping with remote sensing: challenges and opportunities, *Int. J. Remote Sens.*, 41, 1555–1581, 2020.